Elastic scattering of ^{16}O by ^{28}Si

V. Shkolnik, D. Dehnhard, and M. A. Franey
J. H. Williams Laboratory of Nuclear Physics, University of Minnesota, Minneapolis, Minnesota 55455
(Received 18 November 1982)

Differential cross sections were measured in small angular steps at forward angles for the elastic scattering of ^{16}O from ^{28}Si, ^{29}Si, and ^{30}Si at $E_{lab}=60$ MeV and from ^{28}Si at six other incident energies between 45 and 63 MeV. The angular position of a peak in the diffraction pattern at $\theta_{c.m.}\cong 75°$ was measured as a function of the incident energy between 55 and 63 MeV in 0.5 MeV steps. Close fits to these angular distributions and those of other authors at energies between 41 and 81 MeV, some spanning the whole angular range up to 180°, and the excitation functions at 90° and 180°, were obtained in an optical model analysis. A consistent description of the data was found by the use of a surface-transparent and parity-dependent potential with a real part able to generate a pocket in the total potential. The real and imaginary strengths depend quite strongly and smoothly on the incident energy. This potential shows a transition from surface transparency to strong absorption as E_{lab} approaches 81 MeV. The ambiguities in the strengths of the potential are discussed. The broad dispersive potential resonances which are present in several partial waves at every energy are also discussed and their relative importance is examined.

[NUCLEAR REACTIONS $^{16}O+^{28}Si$, $^{16}O+^{29}Si$, $^{16}O+^{30}Si$, $E=45-63$ MeV, measured $\sigma(E;\theta)$. Optical potential fit, $E=41-81$ MeV. Parameter ambiguities, parity dependence, potential resonances.]

I. INTRODUCTION

Even after two decades of effort, the understanding of heavy-ion nucleus scattering at low energies is much less satisfactory than our understanding of the scattering of light ions from nuclei. There is no general agreement as to the heavy ion systems for which the elastic and inelastic scattering can be described by either strongly absorbing potentials (SAP) or by potentials which are transparent in the surface (STP), as to whether these potentials are energy dependent or not, or even whether the interaction between heavy ions can be adequately represented by a potential. It is not clear, for example, whether the successful application in some instances of potentials derived from folding procedures is genuine, or true only for some systems or for data limited in angular range. There still exists, in connection with these and other forms of potentials, the problem of how to formulate the criteria which distinguish acceptable fits from those which are not acceptable. As a result, the same elastic scattering data are often fitted with very different potentials, or subjected to qualitatively different interpretations.

For example, angular distributions for the elastic scattering of ^{16}O and ^{28}Si have been fitted previously *in the average* (neglecting intermediate angle oscillations) from $E_{lab}=33$ to 66 MeV and *closely* (reproducing the oscillations) at 142.5 and 215.2 MeV with an energy-independent, shallow real but strongly absorbing potential of Woods-Saxon shape, known as potential E18.[1] Fits of similar quality were obtained for the same data by use of a very deep real potential derived from double folding together with an energy-dependent phenomenological imaginary part.[2]

In an attempt to better define the optical potential, we initially made very detailed measurements[3] of the elastic scattering of ^{16}O from $^{28,29,30}Si$ at $E_{lab}=60$ MeV. These data revealed large oscillations in the cross sections for $\theta_{c.m.}>55°$ which were not amenable to an optical model analysis with strongly-absorbing potentials[3] but were closely reproduced with surface-transparent potentials.[4] Subsequently, complete angular distributions measured for $^{16}O+^{28}Si$ at $E_{lab}=50.0$ and 55.0 MeV showed large cross sections at the far backward angles.[5,6] Instead of fitting these expanded data with a potential, the authors of Refs. 5 and 6 modified the matrix elements of the potential E18 by the addition of a single Regge pole whose position and width in angular momentum space varied with the incident energy. This approach yielded good fits at these two energies. However, it was shown that the same data could be fitted as well with STP,[7-9] with STP having l-dependent absorption,[10] and also with a weakly absorbing potential using an ingoing wave boundary condition.[11] Systematic fitting of large angle data of Refs. 5 and 6 and the angular distributions measured[10] by us at the forward angles in the interval $45.0\leq E_{lab}\leq 63.0$ MeV showed that simultaneous close fits at all these energies could be obtained[10] only by introducing into an STP a smooth energy dependence for its real and imaginary strengths. The use of the l dependence in the absorption facilitated the fitting of the enhanced cross sections at the very large angles. Similar conclusions about the potential's energy dependence were reached in an analysis[12,13] of the scattering of ^{16}O from $^{24,26}Mg$.

The measurements of the 180° excitation function[14] (180° EF) created a new situation since none of the previously considered potentials could explain the prominent gross structure which it contains. The authors of Ref. 14 suggested that each of the peaks in the excitation function is caused by a potential resonance involving one or a few partial waves, but no fit to the data was presented. One

attempt[15] was made to fit the excitation function together with the two complete angular distributions by an optical potential. Although the angular distributions and the approximate positions of the peaks of the excitation function were reproduced reasonably well, the strongly oscillatory behavior of the excitation function was not fitted. We have shown[16] that this failure to reproduce the excitation function can be remedied by introducing a small parity dependence into the STP, that is by multiplying the potential strengths by $[1+C(-1)^l]$ for each partial wave l. C is the coefficient of the parity dependence.

We have also shown[17] that reasonable agreement with the angular distributions and 180° EF can be obtained from a very simple inelastic transfer model. Addition of a ^{12}C transfer amplitude, calculated in the distorted wave Born approximation (DWBA), to the potential scattering amplitude produced a good representation of the period and magnitudes of the peaks in the excitation function.

In this paper we give experimental details on the acquisition of our $^{16}O + Si$ data, a fraction of which has been previously presented in Refs. 3 and 10. We then discuss the properties of our STP, which fit the observed strong diffractionlike patterns in the angular distributions which SAP do not. We further show the sensitivity of the STP fits to small changes in the optical parameters and present details of the calculations with a parity- and energy-dependent STP which produce a close fit to the 180° EF and good fits to the angular distributions.

We report on our principal new result, an energy-dependent potential which closely reproduces all $^{16}O + ^{28}Si$ elastic data known to us between $E_{lab}=41$ and 58 MeV and angular distributions at forward angles up to 81 MeV. This potential is strongly absorbing in the interior and shows a transition from transparency to strong absorption in the surface as E_{lab} approaches the higher end of this range.

We also discuss the ambiguities present in the real and imaginary well depths. The nature of the resonances inherent in this potential are described and their relative importance is investigated. Finally, we present experimental data which point to the limits of the applicability of the potential.

II. EXPERIMENTAL RESULTS

A. Data taken at Minnesota

We have measured differential cross sections for the elastic scattering of ^{16}O from ^{28}Si, ^{29}Si, and ^{30}Si in the interval $8° \leq \theta_{lab} \leq 52°$ using an ^{16}O beam from the University of Minnesota MP Tandem Van de Graaff accelerator. Data were taken for ^{28}Si, ^{29}Si, and ^{30}Si at $E_{lab}=60.0$ MeV in steps of 0.5° and for ^{28}Si at six additional energies, $E_{lab}=45.0$, 50.0, 55.0, 57.0, 58.0, and 63.0 MeV, in steps of 0.67°. Some of the results, shown in Figs. 1 and 3–6 as solid dots, have been presented[3,10] previously.

The targets consisted of self-supporting silicon dioxide foils, about 50 to 60 $\mu g/cm^2$ thick and enriched in ^{28}Si (99.58%), ^{29}Si (92.0%), and ^{30}Si (95.5%). The SiO_2 was reduced in part to SiO during the evaporation from a tantalum boat. The target thickness was monitored by a stationary solid-state detector placed at −30°. At all energies, except 60 MeV, the effects of the target deterioration were minimized by continuously rotating the target in the beam.

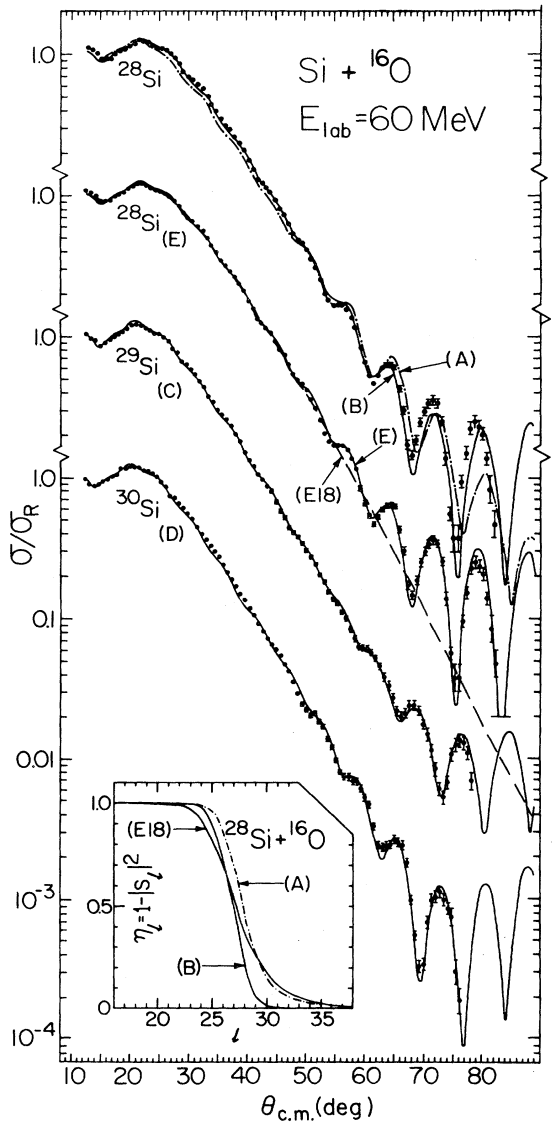

FIG. 1. Differential cross sections σ divided by the Rutherford cross sections σ_R for elastic scattering of ^{16}O from $^{28,29,30}Si$ at $E_{lab}=60.0$ MeV. The curves labeled A, B, C, D, E, and E18 were obtained with the corresponding parameter sets of Table I. Insert: Absorption coefficients $\eta_l = 1 - |S_l|^2$ for parameter sets A, B, and E18.

At the far forward angles ($8° \leq \theta_{lab} \leq 35°$) a split-pole magnetic spectrograph was used. The lack of a target backing made it necessary to detect all important charge states since the charge-state fractions were not equilibrated. For this reason three position-sensitive solid-state detectors were placed along the focal surface of the spectrograph, to collect simultaneously the three charge states (6^+, 7^+, and 8^+) of the ^{16}O ions. Contributions from the 5^+ charge state were measured and found to be negligible. Thus all important charge states were included in calculating the yields. Use of the spectrograph at forward angles allowed a clean separation of the elastic silicon peak from

those due to the oxygen, carbon, and small amounts of tantalum in the target.

Data from $\theta_{lab}=30°$ up to about 52° were taken by an array of six ordinary surface-barrier detectors placed 2° apart and positioned 16 cm from the target. At all angles the angular acceptance of the spectrograph and of each of the Si array detectors was 0.5°. The spectrograph data were normalized to the detector-array data in the overlap region, $30° \leq \theta_{lab} \leq 35°$. The elastic scattering of ^{16}O from the Ta contamination, which is pure Rutherford scattering (σ_R) at 60.0 MeV, served as a further check on the overall efficiency of the system. When using the detector array, background made the largest contribution to the relative experimental errors, which are $\sim 2\%$ at 30° and $\sim 10\%$ at 50°.

Absolute cross sections σ were derived from a normalization of the data at the far forward angles to the optical model predictions. At these angles the predicted σ differ at most by 10% from σ_R, and different potential sets which provide satisfactory fits to the angular distributions yield cross sections that agree to within about $\pm 3\%$. An additional error of $\pm 5\%$ results from an uncertainty of $\pm 0.2°$ in the scattering angle so that the overall error in the absolute normalization is estimated to be $\pm 6\%$.

With the six-detector array we have also measured, in 0.5 MeV steps between 55 and 63 MeV, the angular position of the ninth peak in the angular distribution (counting the top of the main rise above $\sigma/\sigma_R = 1$ as the first peak in the diffraction pattern). The ninth peak was chosen because it provided the best combination of peak to valley ratio and counting rate. These data and their analysis are presented in Sec. III H.

B. Data from other laboratories

Differential cross sections for the elastic scattering of ^{16}O from ^{28}Si have also been measured at other laboratories. Complete angular distributions at $E_{lab}=50.0$ (Ref. 5) and 55.0 (Ref. 6) MeV were measured by Braun-Munzinger *et al.*, and at $E_{lab}=41.23$ MeV by Gelbke *et al.*[18] A 180° excitation function was obtained by Barrette *et al.*[14]

These three angular distributions, like those obtained by us, have pronounced oscillatory patterns, first found by Siemssen *et al.*[19] The work of Cramer *et al.*[1] concentrated on the gross features of the data in a wide energy range from $E_{lab}=32.7$ to 215.2 MeV, disregarding the oscillations between 32.7 and 81 MeV. Subsequent data taken by Cramer *et al.*[20] confirmed the existence of distinct oscillations between $E_{lab}=40$ and 76 MeV. Very recently, three complete angular distributions[21] were obtained at $E_{lab}=33.2$, 35.7, and 38.2 MeV.

In the present work only angular distributions between 41.23 and 81 MeV are considered, together with the 180° excitation function (180° EF) (Ref. 14) ($30.5 \leq E_{lab} \leq 58$ MeV) and the excitation function at $\theta_{c.m.}=90°$ (90° EF), measured by Kubono *et al.*[22] in the energy interval $30.5 \leq E_{lab} \leq 70$ MeV. The elastic scattering data[23] for $^{16}O + {}^{28}Si$ at $E_{lab}=73.5$ MeV were also fitted but are not presented here because of their limited angular range.

Our forward angle data at $E_{lab}=55.0$ MeV are in very good agreement with those of Refs. 1 and 19, and at $E_{lab}=45.0$ MeV our data are in excellent agreement with those from Ref. 20.

At $E_{lab}=50.0$ and 55.0 MeV we have combined our forward-angle data ($\theta_{c.m.} \leq 78°$) with the data of Refs. 5 and 6 taken at larger angles ($78° \leq \theta_{c.m.} \leq 178.4°$). Our data at 50 MeV for $\theta_{c.m.} > 40°$ are systematically lower than the data of Ref. 5 by $\sim 20\%$. Therefore we renormalized the results of Ref. 5 by a factor of 0.80. This renormalization of the large-angle data was not done at 55.0 MeV since our data and those of Ref. 6 are in agreement around 78°.

Another normalization problem was encountered when the 180° EF of Barrette *et al.*[14] became available. These data were taken with a target of ~ 100 $\mu g/cm^2$ thickness and a laboratory aperture of 80 mrad (horizontal) by 100 mrad (vertical). If the experimental angular distributions from Refs. 5 and 6 (normalized by us at 50 MeV by a factor 0.8 and unchanged at 55 MeV) are averaged over this aperture, the resulting cross sections are only about one third of the values obtained in the measurement of the excitation function at the corresponding center-of-target energies. It has been proposed[24] that this discrepancy is due to the intermediate structure observed in the excitation function, and the use of targets of different thickness in the experiments of Refs. 5, 6, and 14. However, the data of Ref. 24, taken near 50 MeV with a thin target (20 $\mu g/cm^2$), do not appear to support this claim. We have therefore renormalized the large-angle parts ($\theta_{c.m.} \geq 150°$) of the angular distributions to the 180° EF data. (In this angular region the experimental technique was different from the one used at the forward angles.) The renormalization factors are 2.9 at 50 MeV (only 2.3 without the previously mentioned factor of 0.8) and 3.1 at 55 MeV. Only when the large-angle data are renormalized can the angular distribution and the excitation function data be fitted simultaneously. No renormalization was done to the angular distribution data of Ref. 18 at 41.23 MeV since the cross sections near 180°, when averaged over the acceptance aperture, yield a value only $\sim 30\%$ lower than that reported in Ref. 14, in contrast to the factors of about 3 mentioned above. We shall, however, also consider the alternative that the three complete angular distributions are correct at the very large angles, but that for energies $E_{lab} \geq 45$ MeV the 180° EF is overestimated by a factor of ~ 3. It will be shown in the next section that the consequences of this alternative leave the essential features of the optical potential unaffected.

III. ANALYSIS OF THE DATA WITH OPTICAL POTENTIALS

A. General remarks

The elastic scattering data were analyzed with the optical model code RAROMP,[25] which was modified for use with heavy ions. The modifications include: composite form factors made of normal Woods-Saxon (WS) shapes together with WS derivatives, various form factors not of WS shape, parity dependence in both real and imaginary parts of the potential, l-dependent smooth cutoff in the imaginary part, averaging of the cross sections over the acceptance aperture at 180°, and computation of elastic scattering from independently derived matrix elements. As in previous work on ^{16}O scattering by lighter tar-

gets,[12,13,26,27] a fit for the elastic scattering of ^{16}O from ^{28}Si, ^{29}Si, and ^{30}Si was judged good if it reproduced not only (a) the average shape of the angular distribution, but also (b) the phase and (c) the amplitude of the diffraction-like structures.

Initially a six-parameter WS form was chosen for fitting our data since for $^{16}O + Si$ a close fit of the strongly oscillatory pattern contains sufficient information to yield at least six independent parameters at one energy. The justification for this statement is as follows: If only a Fresnel-type average shape of the angular distribution is measured, the position, the width, the amplitude of the main rise above σ_R, and the slope of the exponential falloff after the main rise can determine at most four parameters of the optical potential. Since the exponential falloff is not smooth but has a superimposed Fraunhofer-type oscillatory structure, three more parameters can be deduced in principle from the position, the period, and the amplitude of these oscillations. Thus the total number of independently determinable parameters is seven, so that a six-parameter potential should be free from parameter ambiguities. If the oscillatory structure in the falloff is ignored, the depth V and half-value radius R of the WS form are usually connected, for constant diffuseness a, by the relation

$$\ln V + \frac{R}{a} = \text{const}$$

of Igo.[28]

When the Sommerfeld parameter

$$\eta = \mu Z_1 Z_2 e^2/\hbar^2 k$$

is of the order of 15 or larger, the oscillatory Fraunhofer-type patterns in the angular distributions become rather weak. Here μ is the reduced mass and k is the wave number. Then the angular distribution shapes are close to simple Fresnel-type diffraction patterns because the scattering is dominated by strong absorption and the Coulomb force. Only the tail of the nuclear potential affects the shape of the angular distributions. Such situations result in "Igo-ambiguous" potentials, precluding the knowledge of where the potential starts to deviate from the exponential form which it has at large radii. The Igo ambiguity can be removed for $\eta \lesssim 10$ by carrying out precise measurements of the elastic cross sections over a sufficiently large range of angles, and then insisting on close fits to the data. In this work ($7.8 \leq \eta \leq 11.0$) angular distributions with oscillatory structures measured over all angles are used to deduce parameters of potential shapes more complicated than the usual six-parameter WS form.

We find that potentials which predict the critical angular momentum l_{cr} to be different ($\geq 1\hbar$) from the grazing angular momentum l_{gr} do not give optimum fits. The l_{cr} is determined by the S matrix such that

$$|S_{l_{cr}}|^2 = 0.5 .$$

The l_{gr} on the other hand is determined directly from the experimental quarter-point angle $\theta_{1/4}$ as defined by

$$\sigma(\theta_{1/4}) = \sigma_R(\theta_{1/4})/4$$

via the classical relationship[29,30]

$$l_{gr} = \eta \cot(\tfrac{1}{2}\theta_{1/4}) . \quad (1)$$

Although $l_{cr} \cong l_{gr}$ appears to be a necessary condition, it is not sufficient for a close fit.

B. Strongly absorbing potentials (SAP)

Extensive searching was first performed on the $^{16}O + ^{28}Si$ data at $E_{lab} = 60.0$ MeV by gridding on the potential depths from 5 to 150 MeV for the real part and up to 60 MeV for the imaginary part using standard diffusivities, a_r and a_i, in the range from 0.5 to 0.8 fm. These diffusivities are characteristic of strongly absorbing potentials. It was found that the angular distributions generated by these strongly absorbing potentials fit the data well "in the average" up to $\theta_{c.m.} \sim 50°$, but completely fail to reproduce the large oscillations beyond. Predictions with such a SAP, E18, are shown in Fig. 1. A similar search using an SAP with an l-dependent smooth cutoff in the imaginary part defined[31] by

$$W(r,l) = W(r)[1 + e^{(l-l_c)/\Delta}]^{-1} \quad (2)$$

also proved fruitless.

If the ratio between the real and the imaginary strengths of a strongly absorbing potential is made large, as in set A of Table I, the oscillations beyond 50° are reproduced to some extent, but at the cost of seriously underestimating the data between the main rise and $\theta_{c.m.} < 50°$ (Fig. 1, curve A). Thus the experimental $\theta_{1/4}$ is not reproduced in this case and l_{gr} differs significantly (by one unit) from l_{cr}. However, having $l_{cr} \cong l_{gr}$ does not guarantee a close fit. For example, at $E_{lab} = 60$ MeV, E18 with $l_{cr} \simeq l_{gr}$ fits the quarter point angle but does not reproduce the oscillatory pattern of the data.

We have also tried fitting the data using potentials with the real and the imaginary parts derived from double folding employing a Gaussian interaction of range 1.4 fm. Independent adjustment of the strengths produced good fits "in the average," but did not fit the oscillatory structure. If charge densities obtained by electron scattering from ^{16}O and ^{28}Si are folded with a Gaussian interaction, the resulting folded potential has a "diffusivity" larger than 0.6 fm which is characteristic of SAP. Attempts[32] to use a real potential from folding, together with a phenomenological absorption of the WS shape, also did not closely fit the oscillations at $E_{lab} = 50.0$ and 55.0 MeV.

In brief, our investigation has shown that, at incident laboratory energies between 40 and 80 MeV, strongly absorbing potentials do not furnish close fits to the elastic scattering of ^{16}O from ^{28}Si, ^{29}Si, and ^{30}Si.

C. Surface-transparent potentials (STP)

The unacceptable fits obtained at 60 MeV with strongly absorbing potentials (SAP) are in contrast to those (curves B–D in Fig. 1) which were obtained using surface transparent potentials (STP) of shallow real depth and relatively weak central absorption. The surface transparent nature of these potentials (sets B–D of Table I) stems primarily from the fact that $a_i < a_r$, whereas $r_i \cong r_r$ and $W < V$. As a consequence, the absorption is only $\sim \frac{1}{20}$ of that of the SAP at the important Coulomb reflection radius R_{cr} as defined by

TABLE I. Optical model potential[a] parameters for $^{16}O + {}^{28,29,30}Si$ elastic scattering at $E_{lab}=60.0$ MeV.

Set	Target	V_r (MeV)	r_r (fm)	a_r (fm)	W_v (MeV)	r_i (fm)	a_i (fm)	$V(R_{cr})$[b] (MeV)	$W_V(R_{cr})$[b] (MeV)	l_{cr}	l_{gr}	χ^2/N
A[c]	^{28}Si	126.04	1.164	0.535	9.84	1.297	0.535	−1.907	−0.567	27.8	26.8	27.0
E18[d]	^{28}Si	10.00	1.350	0.618	23.40	1.230	0.552	−1.253	−0.768	27.2	26.8	18.3
B	^{28}Si	26.10	1.359	0.434	4.88	1.403	0.161	−1.720	−0.017	27.0	26.8	5.4
C	^{29}Si	27.55	1.359	0.447	5.24	1.409	0.184	−1.796	−0.037	27.9	27.7	1.9
D	^{30}Si	25.325	1.395	0.410	5.26	1.423	0.158	−2.124	−0.029	29.0	28.6	5.5
E[e]	^{28}Si	27.55	1.346	0.432	7.397	1.379	0.185	−2.746	−0.027	26.9	26.8	2.5

[a] $V(r)=V(r)+iW(r)=V(r)+i[W_V(r)+W_D(r)]$
$=-V_r f(r,R_r,a_r)+i[-W_v f(r,R_i,a_i)+4a_d W_d \frac{d}{dr} f(r,R_d,a_d)]$
where $f(r,R,a)=(1+e^{(r-R)/a})^{-1}$, $R=r(A_1^{1/3}+A_2^{1/3})$, and $r_{Coul}=1.0$ fm (uniformly charged sphere) for all sets. For this table, $W_d=0$.
[b] $R_{cr}=8.7$ fm.
[c] Reference 3.
[d] Reference 1.
[e] Parameters of the l dependence [Eq. (2)] are $l_c=27.0$ and $\Delta=0.8$.

$$R_{cr}=\frac{\eta}{k}\left\{\left[1+\frac{l_{cr}(l_{cr}+1)}{\eta^2}\right]^{1/2}+1\right\}. \quad (3)$$

We prefer the term "Coulomb reflection radius" over the more common "strong absorption radius" since the latter is misleading for STP which have only very little absorption at R_{cr}. The transparency for the surface partial waves may be further enhanced by making the absorption also l dependent, as in Eq. (2), for example. Set E (Table I) gives $W(R_{cr}=8.7\text{ fm})=27$ keV but, due to the l dependence, the effective absorption for the grazing partial wave $l=27$ at 60.0 MeV is only 13.5 keV. This l-dependent set generates the excellent fit shown in Fig. 1 (curve E).

Table I shows that sets B–E satisfy the condition $l_{cr}\cong l_{gr}$. Another important property of these potentials is that their real parameters produce a "pocket" in $V_{tot}(r,l)$ (in contrast to E18), where

$$V_{tot}(r,l)=V(r)+V_{Coul}(r)+\frac{\hbar^2}{2\mu r^2}l(l+1)\,. \quad (4)$$

The presence of the "pocket" will cause, for some partial wave l, an abrupt change in the classical distance of approach r_{min} given by the relationship

$$E_{c.m.}=V_{tot}(r_{min},l)\,. \quad (5)$$

For sets B–E this discontinuity in r_{min} occurs for $l\cong l_{cr}$.

When $V_{tot}(r,l)$ is plotted as a function of r, one finds that for sets B–E, $E_{c.m.}$ is tangential to $V_{tot}(r,l_{cr})$ at $r=r_b$, the barrier top radius. Figure 2 shows the shape and relative position of the "pocket" in V_{tot} for set B at $E_{lab}=60.0$ MeV, where $l_{cr}=27.0$. It is our experience that at a given $E_{c.m.}$ only those STP satisfying the conditions $l_{cr}\cong l_{gr}$ and $E_{c.m.}\cong V_{tot}(r_b,l_{cr})$ generate close fits to oscillatory angular distributions measured over an extended range of angles. Equation (5) in the form $E_{c.m.}=V_{tot}(r_b,l)$ is sometimes quoted[33,34] as the condition for a barrier-top orbiting resonance (for partial wave l). We show later that a picture involving the dominance[34] of a single resonating

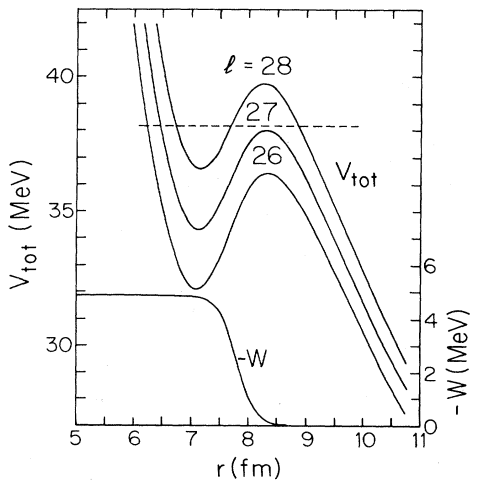

FIG. 2. Total potential energy $V_{tot}(r,l)$ [Eq. (4)] for $l=26$, 27, and 28 and the absorption $-W(r)$ of set B. The broken line, $E_{c.m.}=38.18$ MeV ($E_{lab}=60$ MeV), is nearly tangential to $V_{tot}(r,l=27)$ at $r=r_b\approx 8.3$ fm, the barrier top radius.

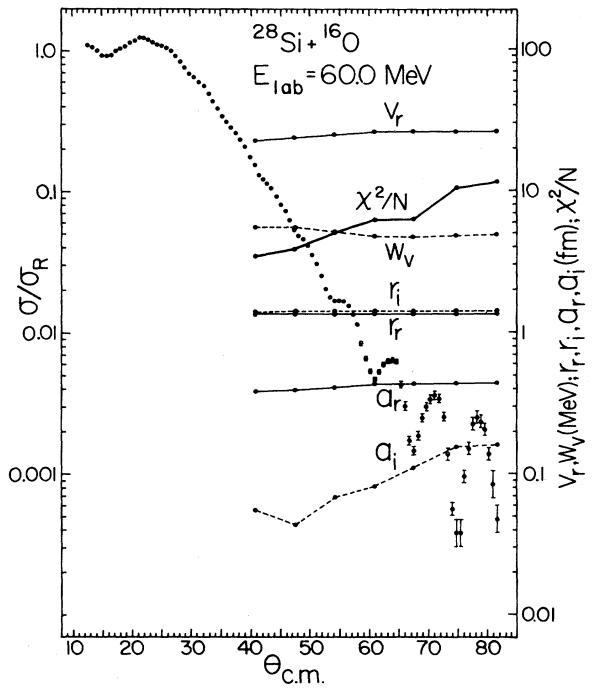

FIG. 3. Data points: σ/σ_R for the elastic scattering of ^{16}O from ^{28}Si at $E_{lab}=60.0$ MeV. Points connected by solid and dashed lines: optical model parameters and χ^2/N as a function of the angle up to which the data were included in the search for a best fit.

partial wave is not confirmed by our potentials.

Another important property of the STP can be seen in the insert of Fig. 1 which compares the absorption coefficients, $\eta_l = 1 - |S_l|^2$, for sets A, B, and E18. The number of partial waves over which the absorption coefficients change from 0.9 to 0.1 is a factor of 2 smaller for the STP B than for E18. We find that close fits require not only that the falloff of the absorption coefficients be centered near l_{gr}, but also that the cutoff *about* l_{cr} must be rather narrow.

We now discuss how well the parameters of our potentials are determined. If the data are limited to $\theta_{c.m.} \leq 40°$, the deduced parameters are "Igo ambiguous." The addition of more data removes the Igo ambiguity and leads to parameter sets with best fit values for all parameters which, except for a_i, change little as the angular range is increased. Figure 3 shows parameters of the optical potential yielding best fits (and the corresponding values of χ^2/N) as a function of the angle up to which the data were included in the search. The best fit imaginary diffusivity a_i starts with a rather small value $a_i \leq 0.1$ fm, and increases as more data are fitted, showing that the very small values $a_i \leq 0.2$ fm arise from the limited extent of the data. It will be demonstrated later (Sec. III D) that fits to angular distributions extending over the whole angular range lead to imaginary diffusivities $a_i \cong 0.3$ fm. Nevertheless, even these more acceptable values of a_i are still considerably smaller than the "standard" value of $a_i \cong 0.6$ fm of the SAP. Similarly, the real diffusivities of the STP cluster around $a_r \cong 0.45$ fm, which is far short of the equivalent diffusivities of double-folding potentials (Sec. III B) and phenomenological potentials such as E18.

In order to estimate the uncertainties in the best fit parameters of set B (Table I), we varied each parameter one by one in small steps, and searched on all of the other parameters until the fits converged. All 60.0 MeV data shown in Fig. 3 were included in the search. The percentage of change in each of the six WS parameters needed to produce (after searching) an increase of 50% in the value of χ^2/N are the following: 15% for V_r, 2% for r_r, 13% for a_r, 22% for W_v, 1% for r_i, and 93% for a_i. These numbers show that the best determined parameters are the two radii and that a_i is poorly determined.

In order to find out how far into the interior changes in the potential affect the fit to the elastic scattering, we used a modified version of the "notch" perturbation method.[35,36] A "notch" of Gaussian shape of width $\alpha = 0.5$ fm (FWHM) was positioned at decreasing values of r. The magnitude of the notch was set equal to $0.05V(r)$ for the real potential and to $0.20W(r)$ for the imaginary potential. For $^{16}O + ^{28}Si$ at $E_{lab}=60.0$ MeV we find that substantial ($>50\%$) changes in χ^2/N occur at values of r as small as 4.5 fm. This is significantly inside the distance of closest approach (6.5 fm) for the grazing partial wave and indicates the sensitivity of the fit to the potential at small distances for this type of STP, which has shallow interior absorption. In Sec. III F we describe our energy-dependent potential with strong interior absorption (but which is otherwise similar to set B) which gives improved fits and is insensitive to changes at such small radii.

Earlier versions of the STP sets B and D (Table I) have been used successfully in a DWBA analysis[37] of $^{16}O + ^{30}Si$ inelastic data and in a coupled-channels analysis[38] of $^{16}O + ^{28}Si$ elastic and inelastic data.

D. Energy dependence of the surface transparent potentials

The elastic scattering data between $E_{lab}=45.0$ and 63.0 MeV presented in this paper (Figs. 4–6), some of which were discussed in Ref. 10, show a systematic shift of the oscillatory pattern toward small angles as the energy is increased. This shift is larger than that predicted by energy independent optical potentials. Free searches with six-parameter WS forms at each of the eight energies produce potentials with nearly equal geometry parameters and a systematic increase of the real and imaginary strengths with energy. The geometry parameters are similar to those of set B in Table I. With the real geometry fixed, the energy dependence of the real depth is very nearly linear. The dependence of the imaginary depth can be taken either as linear, if the imaginary radius is allowed to increase linearly with the energy while the diffusivity a_i is kept constant or, equivalently, as quadratic (or exponential) if both r_i and a_i are kept constant. The increase in the real well depth with energy maintains a nearly constant depth of the pocket in $V_{tot}(r, l_{gr})$ over the whole energy range. However, the width of the pocket for l_{gr} decreases with increasing incident energy.

The complete angular distributions at $E_{lab}=50.0$ and 55.0 MeV can be also closely fitted with such STP, provided that the imaginary diffusivity a_i is increased from

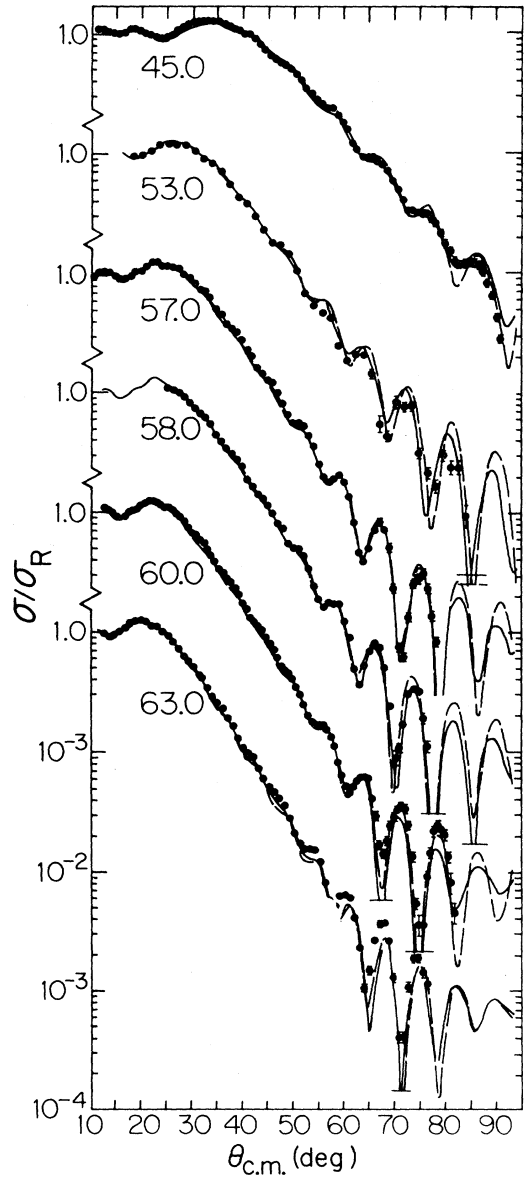

FIG. 4. σ/σ_R for $^{16}O + ^{28}Si$ at $E_{lab}=45.0$, 53.0, 57.0, 58.0, 60.0, and 63.0 MeV. Dashed lines: fits with potential set G (Table III); solid lines: set H (Table III) with modified energy dependence for $E_{lab} \geq 57.0$ MeV (Sec. III F). Data from this work, except for $E_{lab}=53.0$, which are from Ref. 1.

$a_i \leq 0.2$ to ~ 0.3 fm, and a small adjustment is made in the imaginary radius r_i. The effect of these adjustments is a reduction of the absorption in the vicinity of the "pocket," resulting in an enhancement of the cross sections at very large angles. This strong dependence of the large angle cross sections on the absorption in the pocket is consistent with the findings of Brink and Takigawa.[39] Using a semiclassical method, they separated the contributions to the cross sections from the inside and from the outside of the potential barrier. According to their results, the cross sections at large angles are mainly due to the contributions from the pocket.

Additional reduction of the absorption of this STP for

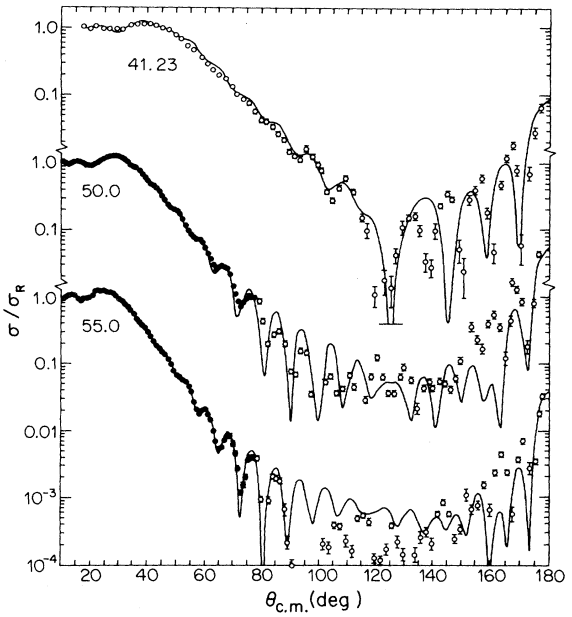

FIG. 5. σ/σ_R for $^{16}O + ^{28}Si$ at $E_{lab}=41.23$, 50.0, and 55.0 MeV. Solid data points: this work; open data points: data of Ref. 18 (41.23 MeV), Ref. 5 (50.0 MeV), and Ref. 6 (55.0 MeV). Solid lines: fits with set G.

partial waves $l \geq l_{gr}$ by means of an l dependence [Eq. (2)] leads to a further increase in the cross sections at very large angles. In Ref. 10 we have shown excellent fits to the angular distributions in the interval $45 \leq E_{lab} \leq 63$ MeV using such l-dependent potentials. The fits shown in Figs. 4–7 were obtained with optical potentials which are energy and parity dependent (but contain no l dependence). These potentials are described in Sec. III E after a discus-

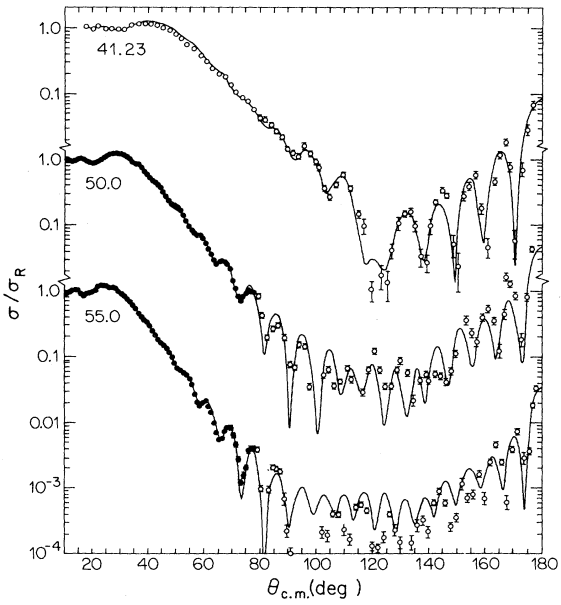

FIG. 6. Same as Fig. 5 except for solid lines which were obtained with best fit potential set H.

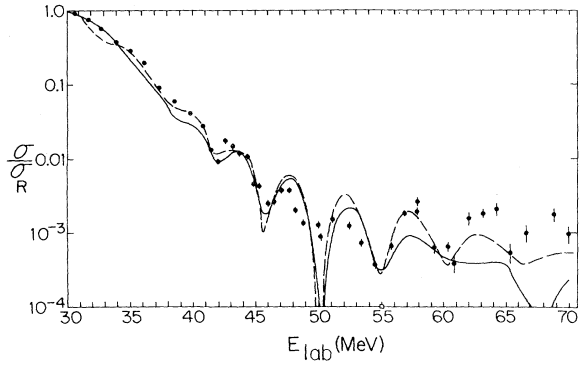

FIG. 7. σ/σ_R for $^{16}O + {}^{28}Si$ at $\theta_{lab}=90°$ as a function of E_{lab} (90° EF of Ref. 22). Solid line: prediction with set H; broken line: prediction with set G.

sion of the 180° EF (Ref. 14) which requires parity dependence for a close fit.[16]

Since the angular distributions are measured up to near 90° in the c.m. and fitted closely and systematically by an (energy dependent) optical potential, it is not surprising that the $\theta_{c.m.}=90°$ EF (Ref. 22) (Fig. 7) is also fitted. This we have verified in the energy interval $45 \leq E_{lab} \leq 63$ MeV by generating the 90° EF from the potential given in Ref. 10. However, a serious problem arises when close fits are sought simultaneously to the angular distributions and the 180° EF (Fig. 8). The difficulties become evident when one tries to fit the 180° EF with an energy-dependent STP like the one given in Ref. 10. For this purpose, the imaginary parameters were made to vary smoothly with energy, and the computed ratio σ/σ_R at 180° was averaged over the acceptance aperture. One finds that $(\sigma/\sigma_R)_{av}$ calculated from such a potential yields peak-to-valley ratios of ~5:4, far short of ~5:1 exhibited by the data. Moreover, in the interval $45 \leq E_{lab} \leq 58$ MeV, $(\sigma/\sigma_R)_{av}$ shows peaks at energies at which consecutive angular momenta become the grazing angular momenta, i.e., approximately twice as many peaks are predicted as are seen in the data. Thus, while the STP from Ref. 10 provides close fits to the angular distributions measured for $45 \leq E_{lab} \leq 63$ MeV, and to the 90° EF even outside this energy interval, it does not fit the gross structure of the 180° EF. We find[16] that close fits to all these data can be achieved if the STP is also made parity dependent by multiplying the well depths by a factor $[1+C(-1)^l]$ (Sec. III E).

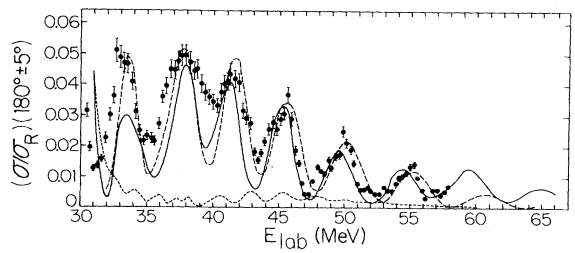

FIG. 8. σ/σ_R for $^{16}O + {}^{18}Si$ at $\theta_{lab}=180°$ (180° EF of Ref. 14). Short-dashed line: calculated with set G, setting $C_r=C_i=0$; long-dashed line: fit with set G (Table III); solid line: fit with set H (Table III).

Alternative descriptions of the gross structure in the 180° EF are of two kinds: The first kind assumes a direct scattering process and regards the peaks in the 180° EF as coming from potential resonances, involving one (or a few) partial waves.[14,15,40–43] According to the second kind,[44] each peak in the gross structure of the 180° EF arises from a number of closely spaced excited states in the compound nucleus ^{44}Ti. This mechanism rests on two further assumptions: (a) A special group of excited states results from barrier-top resonances and the quasimolecular structure of the intermediate scattering system. (b) These configurations are only weakly coupled to other states, and feed preferentially back into the elastic channel, instead of into other channels.

Neither type of description has led to satisfactory fits to the 180° EF. The angular distributions at energies corresponding to peaks in the EF have shapes at large angles like $|P_l(\cos\theta_{c.m.})|^2$, where $l \sim l_{gr}$. These values of angular momentum (Table II) differ by at least two units for consecutive peaks. Descriptions of the first type do not explain the lack of peaks corresponding to consecutive values of l. The second kind of description is unattractive since the 180° EF for elastic scattering of $^{12}C + {}^{28}Si$ and $^{16}O + {}^{40}Ca$, corresponding to the compound systems ^{40}Ca and ^{56}Ni, respectively, also have well-defined gross structures[22,45] similar to those in the $^{16}O + {}^{28}Si$ 180° EF. We believe that these similarities are more likely to stem from a common underlying phenomenon such as exchange effects (leading to a parity dependence) rather than to be related to the very different spectra of the three compound systems.

E. Parity dependence of the optical potential

It has been known for some time that in the scattering of lighter incident ions the exchange effects arising from the Pauli principle lead to exchange terms in the effective optical potential of the Wigner and Majorana types. Calculations[46,47] based on the resonating group theory (RGT) show that these effects can be approximately accounted for by adding to the direct potential the exchange term

$$V_{ex}(r,l)=V_a(r)+(-1)^l V_b(r) . \quad (6)$$

The Wigner-type term $V_a(r)$ represents mainly the exchange of one nucleon. It has an appreciable magnitude when compared with the direct potential but is of shorter range. Its contribution to the cross section is limited to forward angles. The Majorana-type term $(-1)^l V_b(r)$ accounts mainly for the exchange of the core cluster, and the RGT calculations estimate $V_b(r)$ to be relatively small and also of short range.

However, even when only a small parity dependent term is included in the optical potential, the partial cancellation of the scattering amplitudes (from consecutive l) close to 180° is considerably reduced. The cancellation can be seen

TABLE II. Values of the grazing (l_{gr}) and of the critical (l_{cr}) angular momenta at the maxima of the 180° EF.

E_{lab}				
(MeV)	41.23	45.0	50.0	55.0
l_{gr}	17.7	19.6	22.2	24.7
l_{cr}	17.3	19.7	22.4	24.8

most clearly for $\theta=180°$ where consecutive $P_l(\cos\theta)$ alternate between $+1$ (even l) and -1 (odd l). Thus, introducing a constant difference between the nuclear potentials for the even and odd partial waves upsets this cancellation.[48] We note, however, that there is no simple relationship between the parity dependent part of the *potential* and the resulting changes in the S-matrix elements (see Sec. IV A).

Core exchange effects are large if the incident and the target nuclei differ by one or a few nucleons. In the present case $V_b(r)$ corresponding to the exchange of the core cluster is expected to be quite small because ^{16}O and ^{28}Si differ by twelve nucleons. Other exchange effects calculated in the Born approximation which contribute to the scattering amplitude either at forward angles, due to the exchange of two or three nucleons, or at the backward angles, due to the exchange of fewer nucleons than the core, are even less important[46] and can be neglected.

Optical potentials with parity dependence have been successfully used in the analysis[47] of experimental data involving light ions. For heavier systems such as ^{12}C + ^{13}C and ^{16}O + ^{18}O, the parity-dependent term has been calculated in the distorted wave Born approximation (DWBA) assuming, respectively, one nucleon[49] and two-nucleon[50] exchange. Similarly, a phenomenological study[51] of the elastic scattering of ^{16}O from ^{20}Ne has pointed to the need for an odd-even exchange term in the effective potential. A microscopic study[43] of the elastic scattering of ^{16}O from ^{28}Si by the generator coordinate method yielded real phase shifts which did not display any parity dependence. These calculations (and many such calculations for heavier systems) are rather crude approximations since they can account only very poorly for the neglect of the large number of open nonelastic channels. Further, the conclusion[43] that the generator coordinate method does not produce a parity dependence in the phase shifts is unconvincing since the 180° EF is not fit and no attempt was made to fit the angular distributions.

We now describe the simultaneous fitting of the angular distributions and the 180° EF using an optical potential with an empirical parity dependence. The effective parity dependence is assumed to be of the form

$$V_{\rm eff}(r,l)=V(r)[1+C_r(-1)^l] +iW(r)[1+C_i(-1)^l]\ . \quad (7)$$

$V_a(r)$ [Eq. (6)] is thus contained in $V(r)$ and $W(r)$ and $V_b(r)$ has been assumed to have the same shape as the parity-independent part of the potential. The (energy-dependent) coefficients, C_r and C_i, then give the relative strengths of the real and imaginary parity dependence. From resonating-group theory,[46] C_r is expected to decline exponentially as the incident energy increases. In fitting we used an energy-dependent STP similar to the one in Ref. 10 but with constant geometries and without the l dependence in W [Eq. (2)].

By gridding on C_r and C_i, and searching on V and W, we find that good simultaneous fits can be generated with the exponential energy dependence for C_r as predicted by theory. We also find that the dependence on C_i is very weak. The real and imaginary strengths of the STP increase linearly and exponentially with energy, respectively. The fits require this particular type of energy dependence when the real and imaginary geometries are kept constant. This potential (with C_i set equal to C_r) is listed as set G in Table III and has been reported elsewhere.[16] The angular distributions generated by it are shown in Figs. 4 and 5, and the 90° and 180° EF are shown in Figs. 7 and 8. Although the values of C_r and C_i are found to be quite small (at $E_{\rm lab}=55.0$ MeV, $C_r=C_i=-0.0020$), as might be expected, they are crucial for fitting the 180° EF. Without parity dependence, the calculated EF has approximately twice as many peaks as the data and inadequate peak-to-valley ratios (Fig. 8.)

Systematic close fits to angular distributions measured up to $\theta_{\rm c.m.}\leq 90°$, where the effects of C_r and C_i are negligible, determine the real part of the potential quite well in the pocket and beyond, and only somewhat less well the absorption. The potential is even more precisely determined by complete angular distributions. With a potential determined by the data at forward angles, fitting of the 180° excitation function requires the sign of C_r to be negative, since a positive C_r produces a predicted excitation

TABLE III. Optical model parameters for ^{16}O + ^{28}Si elastic scattering at energies $41\leq E_{\rm lab}\leq 63$ MeV. All energies and potential strengths are in MeV; the reduced radii and the diffusivities are in fm.

Set G
$V_r=0.453E_{\rm lab}+1.715$, $r_r=1.323$, $a_r=0.485$
$W_v=0.0082\exp[0.905(E^*)^{1/2}]$, $r_i=1.350$, $a_i=0.300$
$C_r=C_i=-0.112\exp(-0.0731E_{\rm lab})$, $r_{\rm Coul}=1.0$
where $E^*=E_{\rm c.m.}+Q=\frac{28}{44}E_{\rm lab}+11.4$
Set H
$V_r=0.453E_{\rm lab}+1.715$, $r_r=1.323$, $a_r=0.485$
$W_v=2V_r$, $r_i=0.890$, $a_i=0.485$
$W_d=0.0696\exp(0.0658E_{\rm lab})$,
$r_d=1.296$, $a_d=0.210-0.310$ (see text)
$C_r=-0.208\exp(-0.0631E_{\rm lab})$, $C_i=0$, $r_{\rm Coul}=1.0$

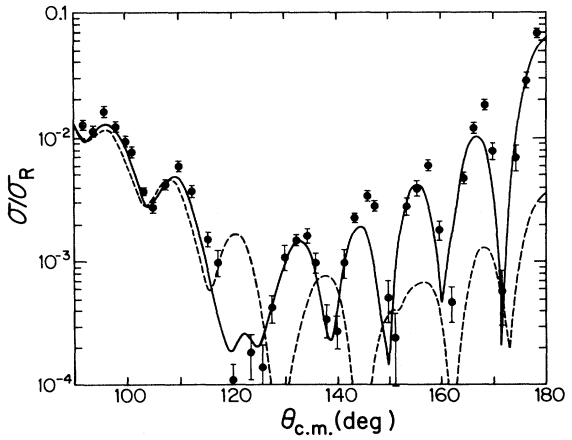

FIG. 9. σ/σ_R for ^{16}O + ^{28}Si at $\theta_{\rm c.m.}\geq 90°$ and $E_{\rm lab}=41.23$ MeV (data of Ref. 18). Solid line: fit with set H ($C_r=-0.0155$); broken line: calculation with set H, setting $C_r=0$.

function out of phase with the data. Setting $C_r=0$ has dramatic effects on the cross sections beyond 90°. This is shown, for example, in Fig. 9 for set H (to be discussed in the next section) at $E_{\rm lab}=41.23$ MeV. Setting $C_i=0$ leaves the quality of the fit almost unchanged. The uncertainties (Sec. III C) in the parameters of set G, given in Table III, are approximately the same as those for set B (of Table I). The cross sections at the very large angles are particularly sensitive to a change in C_r or, equivalently, to a relatively smaller change in W_v. For example, at $E_{\rm lab}=55.0$ MeV σ (180°) is reduced to one third by a 20% increase in W_v or by a 60% decrease in C_r.

F. Potential with composite absorption

Fits generated by set G for the three complete angular distributions (Fig. 5) have several shortcomings: (1) At $E_{\rm lab}=50.0$ and 55.0 MeV the calculated cross sections at $\theta_{\rm c.m.}\sim 100°$ are too large. (2) The last three peaks in these angular distributions are not equally well fitted, in contrast to the fit with an l-dependent absorption,[10] the peak near 160° being especially low. (3) The angular distribution based on set G at $E_{\rm lab}=41.23$ MeV has only four peaks at the very large angles, one less than the data.

Since the forward angle diffraction pattern is closely reproduced in all angular distributions in the interval $45\leq E_{\rm lab}\leq 63$ MeV, we conclude that the real part of the optical potential is well determined.[52] Indeed, we find that these deficiencies are reduced[53] by changing only the imaginary potential in the region of the pocket and in the interior. Extensive searching resulted in the excellent fits to the complete angular distributions shown in Fig. 6. Set H has the same real part as set G, but a composite absorption made of a WS interior (W_v,r_i,a_i) part and an independent WS derivative (W_d,r_d,a_d) peak in the surface, centered at $R_d=7.2$ fm. The increase in the interior absorption required an increase in the magnitude of the parity dependence parameter C_r. For example, at $E_{\rm lab}=55.0$ MeV, C_r is -0.0065 for set H, compared to -0.0020 for set G. In set H, C_i has been set to zero at all energies. All parameters of the imaginary geometry are constant except a_d, the diffusivity of the WS derivative.

We note that the additional imaginary WS derivative peak of set H is very similar to the (l-dependent) polarization potential[54] which results from coupling to excited states of the colliding nuclei. Although the determination of the composite absorption here was done empirically, it is interesting that the search determined the optimum radius ($R_d=7.2$ fm) to be very close to the half-value radius of the real potential ($R_v=7.35$ fm). Calculation[54] of the imaginary polarization potential places it near this radius when the coupling is of collective form. Furthermore, since the real polarization potential is smaller[54] relative to the bare real potential and is located somewhat inside the bare potential half-value radius, it is reasonable that we have found no need for a surface peaked term in the real part of the potential. The magnitude of the surface peak (set H) is similar to that from calculations we have done for the polarization potentials of partial waves around $l_{\rm gr}$ including collective coupling to the first excited state of ^{28}Si.

In fitting the data it was found that there is some ambiguity between the two imaginary diffusivities a_i and a_d

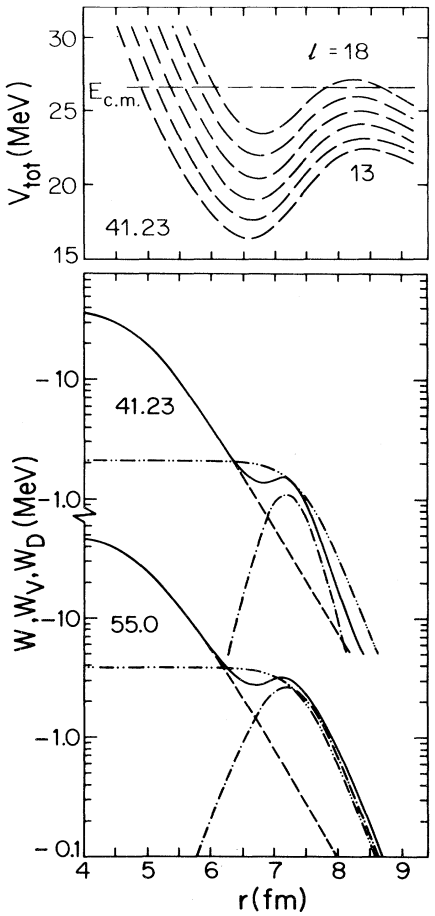

FIG. 10. Top: total potential energy $V_{\rm tot}(r,l)$ [Eq. (4)] between $l=13$ and 18 for set G (same as for set H) at $E_{\rm lab}=41.23$ MeV. Bottom: dashed-double-dotted lines: $-W(r)=-W_V(r)$ for set G at $E_{\rm lab}=41.23$ and 55.0 MeV; dashed lines, dashed-dotted lines, and solid lines are $-W_V(r)$, $-W_D(r)$, and the sum $-W(r)=-W_V(r)-W_D(r)$, respectively, of set H.

and the strength of the surface absorption W_d. Good fits were obtained between 40 and 58 MeV with $W_v=2V_r$, $a_i\equiv a_r=0.485$ fm, $r_i=0.89$ fm, and $r_d=1.296$ fm. An exponentially increasing energy dependence was required for W_d and a linear energy dependence was indicated for a_d, which increases from 0.21 fm at $E_{\rm lab}=41.23$ MeV to 0.310 fm at $E_{\rm lab}=50.0$ MeV. Above 50 MeV, a_d is constant. The composite absorption with its interior and surface components is shown in Fig. 10 for $E_{\rm lab}=41.23$ and 55.0 MeV. It is readily seen that the surface part of the composite absorption (set H) is similar to that of potential G, but there is considerably more absorption in the interior. For $E_{\rm lab}=41.23$ MeV the upper part of Fig. 10 shows the positions of the "pockets" and barrier tops of $V_{\rm tot}$ [Eq. (4)] for partial waves $13\leq l\leq 18$. The reduced absorption of set H near the center of the pocket is important in removing the deficiencies (1)—(3).

Set H also generates close fits to the angular distributions measured at $E_{\rm lab}=66.0$, 69.0, and 72.0 MeV,[1,20] if

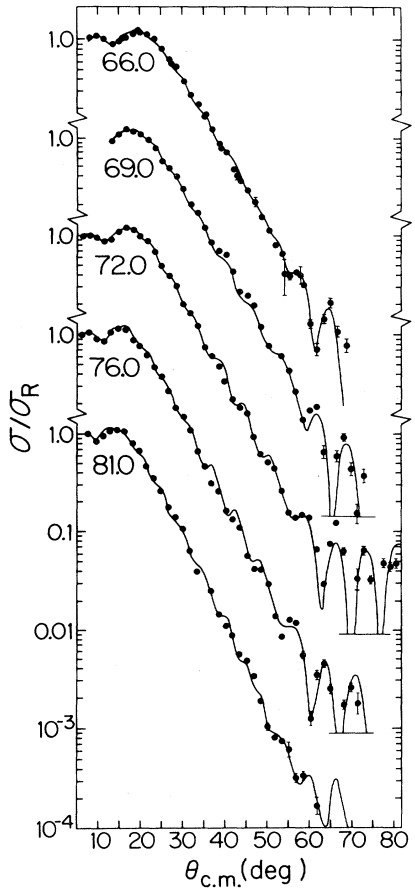

FIG. 11. σ/σ_R for $^{16}O + {}^{28}Si$ at $E_{lab}=66.0$, 69.0, 72.0, 76.0, and 81.0 MeV (data of Ref. 20). The fits were obtained using the real part of optical potential H and the $W(r)$ shown in Fig. 13.

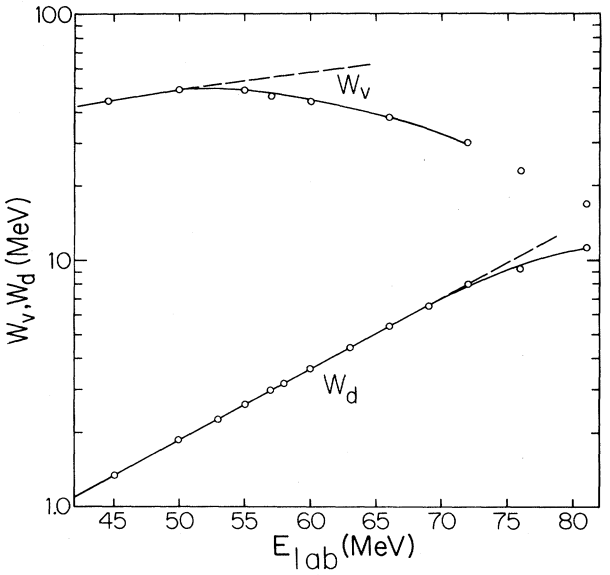

FIG. 12. Energy dependence of the strengths of the composite absorption. Broken lines: set H (Table III); open dots: best fit values, connected by solid line. The two points not connected by a solid line are the central values of the absorption (solid lines in Fig. 13) obtained from a more complicated shape (see text) than used at the lower energies.

modifications are made in the energy dependence of W_v and W_d. Fits to the angular distributions with this modified absorption are shown in Fig. 11. The modified energy dependences for W_v and W_d are shown as the solid lines in Fig. 12. The dashed lines represent the energy dependence of W_v, W_d as given by the formulae in Table III. Even angular distributions between 57 and 63 MeV (E_{lab}) for $\theta_{c.m.} \geq 60°$ are improved somewhat by this modification, but below 57 MeV its effects are negligible. Predictions at these energies with the modified composite absorption are shown in Fig. 4 as the solid lines.

The modified total absorption $W(r)$ for the three energies $E_{lab}=66.0$, 69.0, and 72.0 MeV are shown in Fig. 13 (solid lines). Also shown as solid lines in Fig. 13 are the best fit $W(r)$ for 76.0 and 81.0 MeV, which have substantially different shapes because of a need for an absorptive tail at $r \geq 9$ fm. This tail and a large interior absorption, in addition to the surface peak centered near 7.2 fm, could not be generated by a simple addition of a volume absorption W_V and a surface absorption W_D as in set H. Fits with such a simple sum lead to the broken lines for 76.0 and 81.0 MeV with unrealistically small absorption inside. When the interior absorptions at these two energies were increased to generate the solid lines of Fig. 13, a somewhat

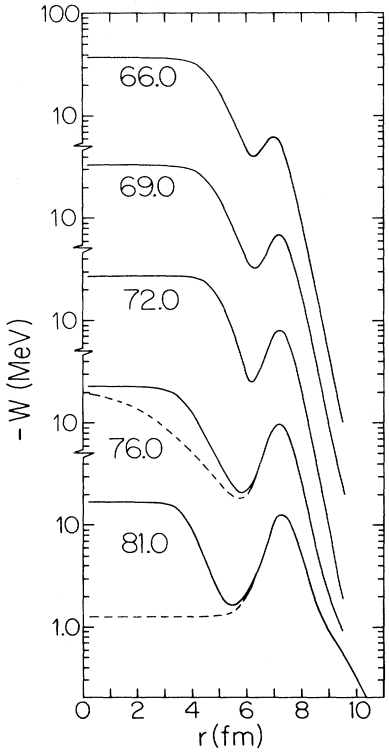

FIG. 13. Composite absorption $W(r)=W_V(r)+W_D(r)$ of the best fit potentials between $E_{lab}=66.0$ and 81.0 MeV (solid lines) and alternative absorptions (broken lines) that yield nearly equivalent fits at the two highest energies.

TABLE IV. Values (in MeV) of the total imaginary potential, $-W(r)=-W_V(r)-W_D(r)$, and of its surface derivative part, $-W_D(r)$, at the Coulomb reflection radius, $R_{cr}=8.7$ fm and $-W_D(r)$ at $r=7.1$ fm (near the center of the pocket) for the modified potential set H (see Fig. 13) at energies $66 \leq E_{lab} \leq 81$ MeV.

E_{lab}	66.0	69.0	72.0	73.5	76.0	81.0
$-W$ (8.7 fm)	0.112	0.22	0.26	0.28	0.45	1.36
$-W_D$ (8.7 fm)	0.096	0.20	0.25	0.26	0.27	0.43
$-W_D$ (7.1 fm)	5.52	6.38	7.76	8.28	9.05	11.4

better fit was obtained than with the $W(r)$ represented by the broken lines. The need for the more complicated shape of the imaginary potential in the surface may be due to the increasing importance of the polarization potentials associated with nuclear reactions, in addition to the inelastic excitations[54] mentioned previously.

The most interesting feature of the radial dependence of $W(r)$ shown in Fig. 13 is the change in character from surface transparency to strong absorption as the energy increases. Table IV lists the values for the absorption at the Coulomb reflection radius, $R_{cr}=8.7$ fm, and at $r=7.1$ fm, the center of the pocket, both for $l=l_{gr}$. At the center of the pocket, near $E_{lab}=76.0$ MeV, the absorption becomes comparable to 8.9 MeV, the value of the absorption of the SAP E18 at this radius $W(7.1\text{ fm})=8.9$ MeV. Similarly, between 76 and 81 MeV, the absorption at R_{cr} approaches and exceeds that of E18.

Since the rise of surface absorption with increasing energy reduces the relative importance of the interior, the dashed lines in Fig. 13 at 76 and 81 MeV generate fits to the data only slightly inferior to those obtained with the solid lines.

The (energy-dependent) real potential does not require any modification up to 81 MeV. However, if the energy dependence of our STP set G or H is used to extrapolate the potential to $E_{lab}=142.5$ and 212 MeV, the data of Ref. 1 are not fitted. Attempts to fit these data with the small real diffusivity ($a_r=0.485$ fm) which was necessary at lower energies were unsuccessful. Best fit potentials (e.g., E18) at the higher energies have values of $a_r \geq 0.6$ fm, have no pocket in V_{tot} for l near l_{gr}, and are strongly absorbing.

As mentioned in Sec. II B there is a discrepancy between the 180° EF data[14] and the results of averaging (over the acceptance aperture) the experimental angular distributions at 50.0 (Ref. 5) and 55.0 MeV (Ref. 6). Since the 180° EF was measured[14,24] twice and no disagreement was reported, we have adjusted the large angle angular distribution data as described in Sec. II B. If, however, it is assumed that the 180° EF is overestimated and that the reported angular distributions are correct, then the latter can be fitted by simply changing the coefficient C_r of set H to

$$C_r=2.60\exp[-0.124E_{lab}\ (\text{MeV})]\ .$$

This new energy dependence does not change the value of C_r at 41.23 MeV, but approximately halves the value at 50 and 55 MeV. Thus, this discrepancy does not affect the essential features of potential sets G or H.

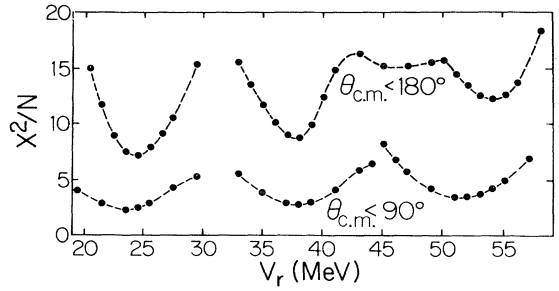

FIG. 14. χ^2 per point as a function of real well depth V_r at $E_{lab}=55.0$ MeV. Upper points: all data were included in the search; lower points: only data for $\theta_{c.m.}<90°$ were included.

G. Ambiguities in the optical potential

Optical potentials are known to be subject to considerable ambiguity, (see, e.g., Ref. 28). We have therefore investigated the ambiguities present in the STP sets C and D (Table I) for $^{16}O+{}^{29,30}Si$ at 60 MeV and in sets G and H (Table II) for $^{16}O+{}^{28}Si$ between 45.0 and 63.0 MeV. For all these cases, the ambiguities in the strength of the real potential were obtained by gridding on the real strength V_r and searching until convergence on all other parameters except C_r and C_i, which were kept constant and equal. The findings which we describe in the following for set G ($^{16}O+{}^{28}Si$) at 55 MeV are typical of the results for the other systems and energies.

Figure 14 shows χ^2/N as a function of V_r. Two sets of searches were done, one including only the forward angle data, $\theta_{c.m.}<90°$, the other including all angles. Distinct minima in χ^2/N were found at values of V_r which are nearly the same for the two cases. We note the following:

(1) The parameters of set G are associated with the first minimum shown near $V_r=24$ MeV and there are no minima for smaller values of V_r.

(2) Equivalent (with respect to χ^2/N) minima are found for depths up to at least 150 MeV.

(3) The spacing in V_r between consecutive minima is about 14 MeV.

(4) There is also a discrete spacing in W_v between consecutive minima, of about 0.7 MeV.

(5) The real and imaginary diffusivities at the minima are nearly constant: $a_r \cong 0.46$ fm, $a_i \cong 0.18$ fm (forward angle data only), and $a_i \cong 0.24$ fm (data at all angles).

(6) As the well depth increases by discrete amounts between minima, the radius decreases according to the relationship

$$\ln V + R/a = \text{const}\ .$$

This is true for both the real and imaginary potentials.

As a result of condition (6), the real potential at and beyond the barrier top ($r_b \approx 8.2$ fm) is the same for all

TABLE V. The differences ΔV and ΔW (MeV) in the real and imaginary well depths between the first few consecutive minima in χ^2/N as a function of E_{lab} (MeV). The Woods-Saxon parameters at each energy can be obtained from this table and set G (Table III) in the manner discussed in the text for $E_{lab}=55$ MeV.

E_{lab}	45.0	50.0	55.0	60.0	63.0
ΔV	11.0	13.0	14.0	15.2	15.7
ΔW	0.55	0.65	0.70	0.72	0.83

minima. However, these equivalent real potentials differ significantly inside the barrier top radius. In particular, the depth of the pocket for l near l_{gr} increases in discrete steps. Each increase produces an additional node in the real and imaginary parts of the radial wave function in the pocket. This corresponds to the presence of an additional potential resonance state.[55] If the absorption is set to zero, increasing V_r by about 14 MeV produces a 180° increase in the real phase shift for l near l_{gr}.

With $V_r \cong 14$ MeV below that for the first minimum (Fig. 14), there is no pocket in V_{tot} (for $l \cong l_{gr}$). The fact that no fits are obtained here [condition (1)] indicates the importance of having a pocket. This is further seen by perturbing V_{tot} in the region of the pocket leaving the barrier top unaffected. In this case, the cross sections forward of $\theta_{c.m.} \sim 60°$ are little changed, but the larger angle oscillations are shifted. This finding, i.e., that the larger angle ($\theta_{c.m.} \geq 60°$) cross sections contain significant contributions from the pocket region, is similar to the result[39] of Brink and Takigawa for the elastic scattering of $\alpha + {}^{40}Ca$.

The discrete increase in W_v [condition (4)] is understandable as a consequence of the need for maintaining a constant mean-free path λ in the middle of the pocket (at $r \sim 7$ fm). Here (with E_{kin} and W in MeV and μ in u)

$$\lambda = 4.6 \left[\frac{E_{kin}(r)}{\mu W^2(r)} \right]^{1/2} \text{fm} , \tag{8}$$

where

$$E_{kin}(r) = E_{c.m.} - V_{Coul}(r) - V_{nucl}(r) .$$

At the minima of Fig. 14, λ is ~ 2 fm in the pocket.

The study of the ambiguities for $^{16}O + {}^{28}Si$ at energies other than 55 MeV has shown that the discrete spacings ΔV and ΔW between consecutive minima increase systematically with energy (Table V). This increase is possibly a result of the larger spacing between resonant states due to the increasingly narrower pocket for l_{gr} as the incident energy increases.

The parabolas obtained in investigating the potential ambiguities for nine-parameter sets such as set H have minima in close agreement with those for six-parameter sets, such as shown in Fig. 14. The nine-parameter parabolas are much shallower due to the greater flexibility provided by the three additional parameters. Between the minima, converged fits obtained with nine-parameter sets are quite acceptable, having χ^2/N within 50% of the best fits. However, constant geometries and smooth energy dependencies for the strengths are obtained only for parameter sets near the minima.

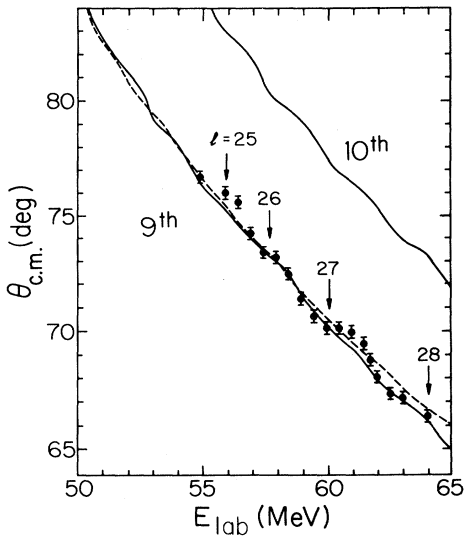

FIG. 15. Angular position $\theta_{c.m.}$ of the ninth and tenth peaks in the angular distribution as a function of E_{lab}. (The maximum value of σ/σ_R in the main rise is counted as the first peak.) The arrows (labeled by l) indicate the energies at which $E_{c.m.}$ is tangential to $V_{tot}(r,l)$ at the barrier top ($r=r_b$). Broken line: calculated with set H; solid lines: calculated with an l-dependent potential close to set 11 of Ref. 10.

H. Possible l dependence in the optical potential

Our STP are able to reproduce the forward angle diffraction patterns measured in 3—5 MeV steps over a wide energy range. However, a detailed (0.5 MeV steps) measurement of the energy dependence of this oscillatory structure revealed an additional feature which is not reproduced by our potentials. The results of the measurement of the angular position of the ninth peak in the angular distribution as a function of incident energy are shown in Fig. 15. We find a pattern of alternating energy intervals over which the peak position changes first very little and then moves forward two to three times more rapidly. This behavior is quite different from that given by simple diffraction models[56] in which the location of a given peak varies smoothly with energy (or equivalently with the wave number k) as

$$kR \sin\theta/2 = \text{const} .$$

The energies around which the peak is nearly stationary ("plateaus") are spaced by approximately 2.5 MeV. This spacing is very close to the difference in centrifugal energy at the barrier top ($r_b = 8.2$ fm) for adjacent angular momenta,

$$\Delta V_{cen} = \frac{2(l+1)\hbar^2}{2\mu r_b^2} . \tag{9}$$

Furthermore, the centers of these plateaus occur at energies at which $E_{c.m.}$ is tangential to the barrier top (sets G and H) for consecutive integer l. These energies and the associated angular momenta are marked by arrows in Fig. 15.

Although sets G and H reproduce the location of the peaks at energies where angular distributions have been

TABLE VI. S-matrix elements $S_l = e^{2i\delta_l}$ for $^{16}O + ^{28}Si$ elastic scattering at $E_{lab} = 55.0$ MeV calculated with set G. All listed values are multiplied by 100.

	$S_l(C_r = C_i = -0.002)$		$S_l^0(C_r = C_i = 0.0)$		$\Delta S_l = S_l - S_l^0$		$\beta = \frac{\Delta S_l}{S_l^0 - 1}$		
l	ReS_l	ImS_l	ReS_l^0	ImS_l^0	ReΔS_l	ImΔS_l	Reβ	Imβ	$\lvert\Delta S_l\rvert$
16	−7.10	−1.41	−7.03	−1.64	−0.070	+0.23	+0.069	−0.23	0.240
17	−5.19	+3.88	−5.03	+4.08	−0.16	−0.20	+0.16	+0.20	0.256
18	+2.90	+6.53	+2.62	+6.54	+0.28	−0.010	−0.28	−0.008	0.280
19	+10.66	+2.71	+10.82	+2.48	−0.16	+0.23	−0.17	−0.26	0.280
20	+12.17	−4.92	+12.30	−4.69	−0.13	−0.23	+0.16	+0.25	0.264
21	+5.75	−4.54	+5.47	−4.49	+0.28	−0.05	−0.29	+0.067	0.284
22	+1.68	+12.34	+1.69	+12.00	−0.01	+0.34	+0.052	−0.34	0.340
23	+17.27	+32.90	+17.57	+33.00	−0.30	−0.10	−0.27	+0.23	0.316
24	+40.25	+39.07	+40.17	+39.20	+0.08	−0.13	−0.19	+0.091	0.153
25	+60.10	+44.64	+60.16	+44.71	−0.06	−0.07	−0.021	−0.15	0.092
26	+85.81	+36.73	+85.72	+36.79	−0.09	−0.06	−0.059	+0.27	0.108
27	+95.66	+22.57	+95.69	+22.52	−0.03	+0.05	+0.24	+0.088	0.058
28	+98.55	+13.46	+98.54	+13.49	+0.01	−0.03	−0.23	−0.050	0.032

fitted, in between these energies they fail to describe the plateaus and subsequent sudden shifts in position [broken line (set H) in Fig. 15]. The only potential for which we have seen this structure is a STP with l-dependent absorption [Eq. (2)]. The solid curves in Fig. 15 were generated using a (smoothly energy-dependent) potential close to Set 11 of Ref. 10. These calculations reproduce the period of the shifts in position but not their magnitude. This set has not been adjusted (by including a parity dependence) to reproduce the 180° EF, but the existence of sudden shifts in the diffraction pattern from use of the l dependence suggests the need for more absorption for partial waves below l_{gr} and less absorption for $l \geq l_{gr}$ than is provided by set G or H.

IV. DISCUSSION OF PARITY DEPENDENCE AND POTENTIAL RESONANCES

A. Parity dependence and S-matrix elements

We have introduced the parity-dependent term $C(-1)^l V(r)$ into the potential in order to fit simultaneously the angular distributions and the 180° EF. The usual optical potential which implicitly includes some effects of antisymmetrization between the projectile and target nucleons is insufficient in this regard for this extensive set of data. Introducing a small $(-1)^l$ term into the potential has been a successful approach to account for this deficiency.

We have investigated the effects of the parity dependent term in the potential on the nuclear S-matrix elements since it is sometimes suggested that such a term leads to an odd-even l staggering in S_l. In Table VI we list the S-matrix elements calculated with set G at $E_{lab} = 55$ MeV with (S_l) and without (S_l^0) parity dependence. Also listed are the changes,

$$\Delta S_l = S_l - S_l^0 ,$$

the fractional changes

$$\beta = \Delta S_l / (S_l^0 - 1) ,$$

and $|\Delta S_l|$ due to including the odd-even term in the potential. It is seen that the magnitudes $|\Delta S_l|$ are of the same order as C_r ($\sim 0.2\%$), but that the real and imaginary parts of ΔS_l do not consistently alternate in sign. Indeed, Mackintosh and Kobos[57] have shown that, in general, the effect of a small change in the optical potential on the S matrix is not simple. We note also that both the real and imaginary parts of S_l^0 have some structure, in contrast to the smooth profile characteristic of SAP. The S-matrix elements from set H (not listed) have less structure since the interior absorption is larger for set H than for set G.

An attempt by Frahn *et al.*[58] to fit the 180° EF and the 55 MeV angular distribution by including an odd-even staggering directly in the S-matrix elements led to a reasonable fit to the EF but failed to reproduce the angular distribution between $\theta_{c.m.} = 40°$ and 80°.

B. Resonances and phases shifts

Currently, there is a great deal of discussion involving partial wave resonances as the source of the structure in both the large angle cross sections and the excitation functions for lighter heavy ion scattering in general and for $^{16}O + ^{28}Si$ in particular. We have shown, in Sec. III E, however, that a systematic fit to the 180° EF and angular distributions at several energies can be obtained without invoking isolated partial wave resonances. Rather, the data can be reproduced by an interference between the scattering amplitude due to a parity independent optical potential and that due to an additional parity-dependent term. In this subsection, we describe in detail the character, location and width of the partial wave resonances which do exist in potential sets G and H and evaluate the relative importance of individual partial waves. It will be shown that at any given energy there are several resonating partial waves whose widths are very broad (~ 1–3 MeV in the c.m. system). These resonances exist naturally in the best fit potentials instead of being introduced *ad hoc*. In the following, we discuss these effects for sets G and H. Set G is typical of other STP (Refs. 9, 10, 12, 13, 15, and 19) deduced from the scattering of ^{16}O by *s-d* shell nuclei in that its real and imaginary parts are rather shallow in the interior. However, set H provides better

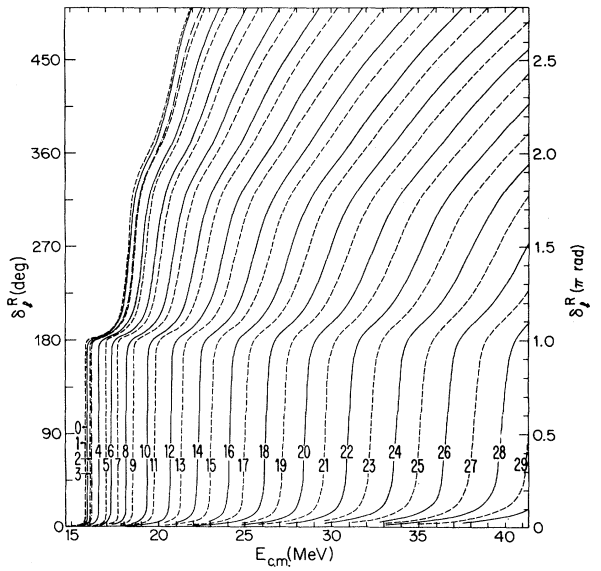

FIG. 16. Real phase shifts δ_l^R for $l=0$–29 as a function of $E_{c.m.}$ calculated with potential set G setting $W=0$.

fits to the data, principally because of the larger interior absorption which makes the $^{16}O + {}^{28}Si$ system opaque at small radii.

Figure 16 shows the energy dependence of the real nuclear phase shift δ_l^R calculated with set G *with the absorption set to zero.* Since the real part of potential set H differs from set G only in the parity dependence, it shows very similar behavior. For this case involving a purely real potential, scattering resonances occur at energies

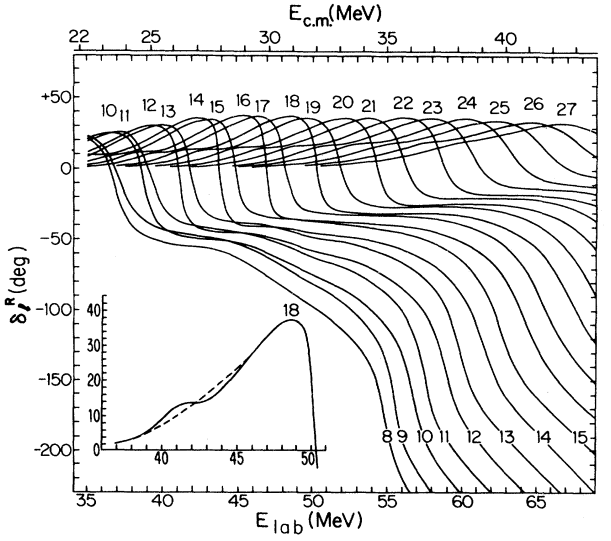

FIG. 17. Real phase shifts δ_l^R as a function of E_{lab} from set H. The values for the partial waves are placed at the respective positive maxima in δ_l^R and also at $\delta_l^R \cong -190°$ for identification. The insert is an enlarged version of $\delta_l^R(E_{lab})$ for the $l=18$ partial wave between 37 and 50 MeV. Note the appearance of a small bump at the energy where $E_{c.m.}$ is tangential to V_{tot} for $l=18$ ($E_{lab}=41.2$ MeV). This is the "remnant" of the $n=0$ potential resonance.

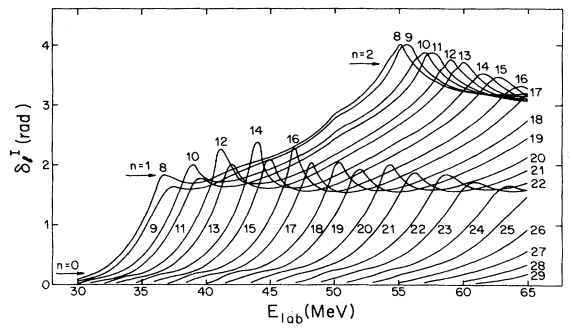

FIG. 18. Imaginary phase shifts δ_l^I in radians from set H as a function of E_{lab}. The numbers give the partial wave l. Also indicated are the series of $n=0$, 1, and 2 potential resonances.

where $\delta_l^R=(n+\frac{1}{2})\pi$, $n=0,1,2,\ldots$. Here $n=0$ refers to the first resonance in the potential neglecting any possible bound states. It is clear that at any energy above the Coulomb barrier, there are several resonating partial waves. For example, at $E_{c.m.}=35$ MeV, the grazing partial wave, $l=25$, is at its first resonance ($n=0$), $l=22$ is at its second resonance ($n=1$), and a range of lower partial waves centered around $l=17$ are near their respective third resonances ($n=2$).

In contrast to the simple potential resonances exhibited by the energy dependence of the real phase shifts calculated with no absorption, the resonances calculated with the full set G or H have a very different character. Due to the presence of absorption, there are no longer any simple potential resonances involving a change of π radians in the phase shift. Instead, the resonances are broadened and strongly damped such that the change in phase shift across the resonance energy is much less than π and most often negative. These features are typical of dispersive resonances[59] at which there is an increased loss of flux to nonelastic channels. The resonances are shifted to higher energy from those of Fig. 16 (with $W=0$).

As discussed in Sec. III F, potential set H removes several shortcomings in the fits with set G by use of a deeper interior absorption and a somewhat larger parity dependence. As can be seen from Fig. 17, this stronger interior absorption produces dispersive resonances for all n and l. Due to the weaker surface absorption of set H, the remnant of the $n=0$ resonance is clearly visible as a modulation of the tail of the $n=1$ resonance (see the insert to Fig. 17). The parity dependence produces a pronounced bunching of the $n=1$ resonance energies for neighboring odd-even partial wave pairs. This bunching decreases with increasing incident energy due to the weakening parity dependence of the potential. In addition to the bunching, the odd-even dependence of the potential also causes a systematic difference in the width of the $n=1$ resonances for odd (wider) and even (narrower) partial waves.

It can be seen from Fig. 18 that the imaginary phase shifts $\delta_l^I(E_{lab})$ have local maxima at the energies where the real phase shifts show resonances. This increased absorption

$$\eta_l = 1 - |S_l|^2 = 1 - e^{-4\delta_l^I}$$

at the resonance energy may be related to the increased

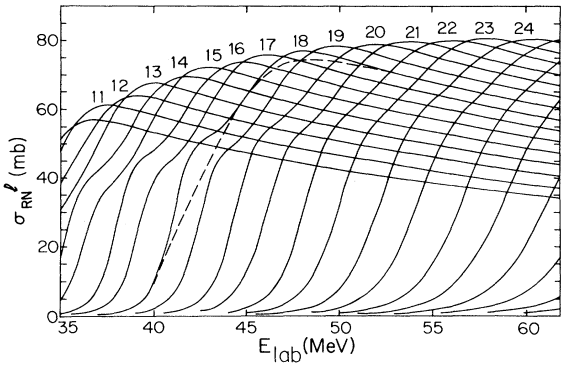

FIG. 19. Calculated reaction cross sections

$$\sigma_{RN}^{l}=\frac{\pi}{k^2}(2l+1)(1-|S_l|^2)$$

for individual partial waves l as a function of E_{lab}. Solid lines: set H; broken line: estimated "background" cross sections without resonance enhancements in σ_{RN}^{l} for $l=18$.

time which the resonating system spends in a region of significant absorption. Indeed, at their respective resonance energies, the slightly more narrow even partial wave resonances (Fig. 17) exhibit stronger absorption than the neighboring odd partial waves which have somewhat larger width, implying a shorter lifetime for the resonance. This alternating strength of the absorption is most clearly seen for the $n=1$ resonances (Fig. 18).

The resonances which are apparent from the energy dependence of the real phase shifts are also seen in the energy dependence of the calculated partial wave reaction cross sections shown in Fig. 19 (set H). An estimated background is shown in Fig. 19 by the dashed line for $l=18$. This background is typical of a strongly absorbing potential without resonances. The rises in cross section above the dashed line occur at the locations of the $n=0$ and $n=1$ resonances (Fig. 19).

It is important to note that the peaks in the 180° EF do not correspond to the positions of individual partial wave resonances in our potential. In fact, the potential resonances are so broad that at any given energy several waves are "resonating." For example (Fig. 17, Set H), at $E_{lab}\cong 55$ MeV, $l=24$, 25, and 26 are passing through the $n=0$ resonance, $l=20$, 21, and 22 through the $n=1$ resonance, and $l=7$, 8, and 9 are passing through the $n=2$ resonance.

One way to assess the relative importance of individual partial waves is to inspect the coefficient a_l in the decomposition of the scattering amplitude,

$$f(\theta)=f_c(\theta)+\sum_{l=0}^{l_{max}} a_l P_l(\cos\theta)\ , \tag{10}$$

where

$$a_l=(2l+1)e^{2i\delta_l^{Coul}}(S_l-1)/2ik\ , \tag{11}$$

and δ_l^{Coul} is the Coulomb phase shift. a_l is a direct measure of the contribution of each Legendre polynomial to the nuclear part of the elastic scattering amplitude such that

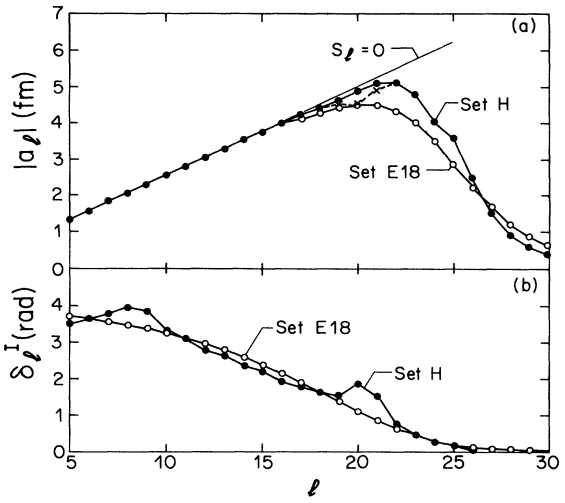

FIG. 20. (a) Modulus of coefficient a_l [Eq. (11)] at $E_{lab}=55$ MeV as a function of partial wave l. Solid dots: set H; open dots: set E18; crosses: calculated with real phase shifts from set H and imaginary phase shifts without resonance enhancement of δ_l^I near $l=20$. Below $l=17$ the differences between $|a_l|$ from sets H and E18 are smaller than the dot size. The thin straight line gives $|a_l|$ for full absorption ($S_l=0$). (b) Imaginary phase shifts δ_l^I at $E_{lab}=55$ MeV as a function of partial wave l. Solid and open dots as in (a). Note the resonance enhancement in δ_l^I from set H near $l=8$ and 20. In both (a) and (b) the calculated values are connected by straight lines.

$$\sigma_{el}^{l,nucl}=4\pi|a_l|^2/(2l+1)\ .$$

For example in Fig. 20(a), we compare $|a_l|$ for E18 and set H at $E_{lab}=55$ MeV. It is apparent that for both potentials, partial waves up to $l\sim 16$ are fully absorbed, i.e., $S_l\cong 0$ so that

$$|a_l|\cong\frac{(2l+1)}{2k}\ ,$$

thereby extinguishing any effect of the $n=2$ resonances in set H. In contrast to E18, this nearly complete absorption continues up to $l=21$ for set H. This effect is due to the stronger attractive real potential of set H (compared to E18) which reduces the distance of closest approach allowing penetration into a region of increased absorption and due to the increased absorption from the presence of the $n=1$ resonances in partial waves around $l=20$ as noted previously. Indeed, the l dependence of the imaginary phase shift δ_l^I [Fig. 20(b)] is smooth for E18 but shows a clear bump near $l=20$ for set H. There is also a bump in δ_l^I for the $n=2$ resonating partial waves around $l=8$; however, the effect of this enhancement in δ_l^I on $|a_l|$ is negligible since the absorption is already complete for these waves. We note that there is no sudden change in $|a_l|$ for any partial wave as might be expected if a particular partial wave were dominating the elastic cross section.

The dashed line in Fig. 20(a) is calculated with δ_l^I of set H modified to eliminate the resonance enhancement between $l=19$ and 22. These modified δ_l^I are essentially equal to those of potential E18. It can be seen that for $l=19$ and 20, the differences in $|a_l|$ between set H and

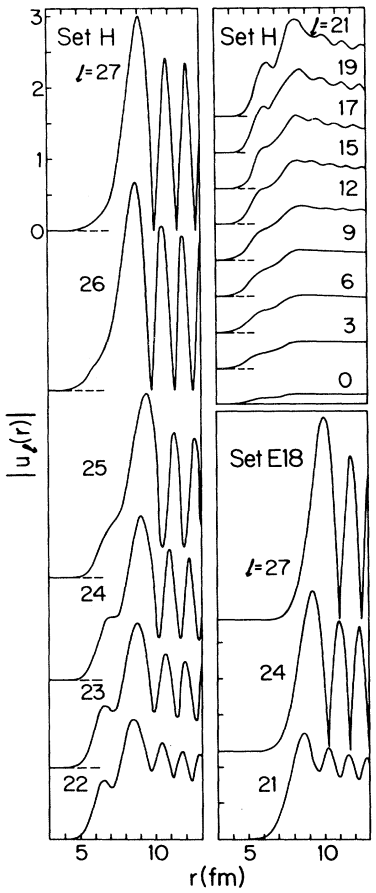

FIG. 21. Modulus of $u_l(r)$, the reduced radial wave functions, calculated for selected l values with sets H and E18 at $E_{lab}=55$ MeV. Relative scale as indicated in the upper left corner.

E18 are almost entirely due to the enhancement in δ_l^I. However, for higher partial waves ($l \geq 23$) the δ_l^I from E18 and set H are similar and thus the larger $|a_l|$ from set H are due to the increasing importance of the *real* phase shift. Potential H contains resonances in the partial waves around l_{gr} (≈ 25), but it is difficult to separate quantitatively the degree to which $|a_l|$ is determined by them or by the qualitatively different nature of the potential. Of course, the a_l are complex and there is interference between the individual terms of the partial wave expansion when computing differential cross sections.

In a recent review article[60] several possible interpretations of the large angle data including potential resonances are discussed. Our detailed fits to the angular distributions and the gross structure in the 180° EF ($E_{lab} \leq 58$ MeV) are the result, in part, of systematic resonant behavior in *several* partial waves and are not due to the dominance of a single resonating wave.

C. Partial wave functions

In addition to analyzing the phase shifts and partial wave reaction cross sections, it is instructive to examine the reduced radial wave functions, $u_l(r)=rR_l(r)$, where $R_l(r)$ is the full radial wave function. Figure 21, for example, shows these wave functions from set H for $^{16}O + ^{28}Si$ at $E_{lab}=55$ MeV. It is clear that the maximum in the wave function does not occur at the barrier top which is located at $r_b=8.2$ fm for l near l_{gr}. For $l=25$, $E_{c.m.}$ is close to the total potential energy at r_b; thus one condition[33] for barrier top orbiting is fulfilled. However, there is no indication of an increased $|u_l|$ at r_b for $l=25$.

Figure 21 also shows that for all waves below $l \approx 26$, there exists an enhanced probability for the system to be in a region centered at the "pocket." This inside peak is clearly absent in the radial wave functions obtained from set E18 (Fig. 21) which has no pocket for l near l_{gr}. We note also the sharp discontinuity in the location of the maximum of $|u_l|$ which occurs between $l=25$ and 26. This sudden shift in position is due to the appreciable sensitivity to the pocket for $l \leq 25$ at this energy (55 MeV).

V. SUMMARY

We have reported detailed measurements of elastic scattering differential cross sections for ^{16}O on the three silicon isotopes at energies above the Coulomb barrier. Systematic close fits have been obtained to these data and the data of other authors for $^{16}O + ^{28}Si$ in the energy interval $41 \leq E_{lab} \leq 81$ MeV using surface transparent and parity dependent optical potentials with energy dependent strengths. The potentials fitting the data for ^{29}Si and ^{30}Si are very similar.

An important feature of the real potential which is necessary for these good fits is the existence of a pocket in the total real potential. This pocket is achieved by a sufficiently large real strength and a relatively small real diffuseness ($a_r \lesssim 0.5$ fm). The optical potential is free from continuous ambiguities but is subject to discrete ambiguities in the potential strengths. The best fit potential (set H) is surface transparent and strongly absorbing in the interior.

A small ($\lesssim 1.5\%$) parity dependence in the real potential was found to be essential for the fit to the 180° excitation function. The simultaneous close fits to the angular distributions and the 180° excitation function unambiguously determine a negative sign for the coefficient of the parity dependent term. This parity dependence is expected to account approximately for antisymmetrization effects which are not included in the local optical potential.

At any energy several groups of broad potential resonances were found to be present, some of which occur for the partial waves $l \ll l_{gr}$ which are completely absorbed so that resonance effects are negligible; others at $l \sim l_{gr}$ and $l \sim l_{gr}-4$ appear to have sizable effects on the scattering amplitudes.

ACKNOWLEDGMENTS

We wish to thank Prof. P. J. Ellis and Prof. Y. C. Tang for valuable discussions, Prof. J. G. Cramer and collaborators for permission to use their data prior to publication, and Prof. D. A. Lewis for use of his folding program. We also thank Prof. J. L. Artz, Dr. S. Kubono, Dr. S. J. Seestrom-Morris, Dr. H. L. Sharma, and Dr. D. J. Weber for their help in data acquisition. The authors are indebted to the Graduate School and the Computer Center of the University of Minnesota for their generous contributions to the large computation costs. This work was supported in part by the U.S. Department of Energy.

[1]J. G. Cramer, R. M. DeVries, D. A. Goldberg, M. S. Zisman, and C. F. Maguire, Phys. Rev. C 14, 2158 (1976).
[2]G. R. Satchler, Nucl. Phys. A279, 493 (1977).
[3]V. Shkolnik, D. Dehnhard, J. L. Artz, D. J. Weber, and M. A. Franey, Proceedings of the Symposium on Macroscopic Features of Heavy Ion Collisions, Argonne National Laboratory Report ANL/Phy-76-2, 1976, p. 761.
[4]V. Shkolnik, D. Dehnhard, J. L. Artz, D. J. Weber, and M. A. Franey, Bull. Am. Phys. Soc. 22, 563 (1977).
[5]P. Braun-Munzinger, A. M. Berkowitz, C. M. Jachcinski, T. M. Cormier, J. W. Harris, J. Barrette, and M. J. LeVine, *Proceedings of the International Conference on Nuclear Structure, Tokyo, Japan, 1977,* edited by the Organizing Committee (International Academic Printing, Tokyo, 1977), p. 616.
[6]P. Braun-Munzinger, G. M. Berkowitz, T. M. Cormier, C. M. Jachcinski, J. W. Harris, J. Barrette, and M. J. LeVine, Phys. Rev. Lett. 38, 944 (1977).
[7]D. Dehnhard, Proceedings of the Symposium on Heavy-ion Elastic Scattering, University of Rochester, 1977, edited by R. M. DeVries, p. 20.
[8]E. H. Auerbach, A. J. Baltz, M. Golin, and S. H. Kahana, see Ref. 7, p. 394.
[9]K. O. Terenetski and J. D. Garrett, Phys. Rev. C 18, 1944 (1978).
[10]V. Shkolnik, D. Dehnhard, S. Kubono, M. A. Franey, and S. Tripp, Phys. Lett. 74B, 195 (1978).
[11]S. Landowne and A. Winther, see Ref. 7, p. 525.
[12]K. Siwek-Wilczynska, J. Wilczyznski, and P. R. Christensen, Nucl. Phys. A229, 461 (1974).
[13]H. T. Fortune, A. Richter, R. H. Siemssen, and J. L. Yntema, Phys. Rev. C 20, 648 (1979).
[14]J. Barrette, M. J. LeVine, P. Braun-Munzinger, G. M. Berkovitz, M. Gai, J. W. Harris, and C. M. Jachcinski, Phys. Rev. Lett. 40, 445 (1978).
[15]S. Y. Lee, Nucl. Phys. A311, 518 (1978).
[16]D. Dehnhard, V. Shkolnik, and M. A. Franey, Phys. Rev. Lett. 40, 1549 (1978); 42, 1574 (1979).
[17]M. A. Franey, V. Shkolnik, and D. Dehnhard, Phys. Lett. 81B, 132 (1979).
[18]C. K. Gelbke, T. Awes, U. E. P. Berg, J. Barrette, M. J. LeVine, and P. Braun-Munzinger, Phys. Rev. Lett. 41, 1778 (1978).
[19]R. H. Siemssen, Proceedings of the Symposium on Heavy-ion Scattering, Argonne National Laboratory Report ANL-7837, 1971, p. 145.
[20]J. G. Cramer, private communication; J. G. Cramer, J. C. Wiborg, Y-D Chan, K. L. Liu, and H. H. Bohn, Nuclear Physics Laboratory Annual Report, University of Washington, 1977, p. 83 (unpublished).
[21]P. Braun-Munzinger, G. M. Berkovitz, M. Gai, C. M. Jachcinski, T. R. Renner, C. D. Uhlhorn, J. Barrette, and M. J. LeVine, Phys. Rev. C 24, 1010 (1981).
[22]S. Kubono, P. D. Bond, D. Horn, and C. E. Thorn, Phys. Lett. 84B, 408 (1979).
[23]I. Tserruya, W. Bohne, P. Braun-Munzinger, C. K. Gelbke, W. Grochulski, H. L. Harney, and J. Kuzminski, Nucl. Phys. A242, 345 (1975).
[24]J. Barrette, M. J. LeVine, P. Braun-Munzinger, G. M. Berkovitz, M. Gai, J. W. Harris, C. M. Jachcinski, and C. D. Uhlhorn, Phys. Rev. C 20, 1759 (1979); J. Barrette, private communication.
[25]G. J. Pyle, University of Minnesota Informal Report No. C00-1265-64, 1964 (unpublished).
[26]J. V. Maher, M. W. Sachs, R. H. Siemssen, A. Weidinger, and D. A. Bromley, Phys. Rev. 188, 1665 (1969).
[27]A. Gobbi, R. Wieland, L. Chua, D. Shapira, and D. A. Bromley, Phys. Rev. C 7, 30 (1973).
[28]G. Igo, Phys. Rev. 115, 1665 (1959).
[29]W. E. Frahn, Ann. Phys. (N.Y.) 72, 524 (1972).
[30]W. E. Frahn, Nucl. Phys. A302, 267 (1978).
[31]R. A. Chatwin, J. S. Eck, D. Robson, and A. Richter, Phys. Rev. C 1, 795 (1970).
[32]G. R. Satchler, Nucl. Phys. A329, 233 (1979).
[33]W. A. Friedman and C. J. Goebel, Ann. Phys. (N.Y.) 104, 145 (1977).
[34]D. Shapira, J. L. C. Ford, Jr., J. Gomez del Campo, R. G. Stokstad, and R. M. DeVries, Phys. Rev. Lett. 43, 1781 (1979).
[35]J. G. Cramer, Bull. Am. Phys. Soc. 20, 1159 (1975).
[36]P. J. Moffa, C. B. Dover, and J. P. Vary, Phys. Rev. C 13, 147 (1976).
[37]A. Dudek-Ellis, V. Shkolnik, J. L. Artz, D. Dehnhard, P. J. Ellis, and H. P. Morsch, Phys. Rev. C 18, 158 (1978).
[38]A. Dudek-Ellis, V. Shkolnik, and D. Dehnhard, Phys. Rev. C 18, 1039 (1978).
[39]D. M. Brink and N. Takigawa, Nucl. Phys. A279, 159 (1977).
[40]S. Landowne, Phys. Rev. Lett. 42, 633 (1979).
[41]S. Kahana, B. T. Kim, and M. Mermaz, Phys. Rev. C 20, 2124 (1979).
[42]V. M. Strutinski, Z. Phys. A 289, 65 (1978).
[43]K. Langanke, Phys. Lett. 104B, 112 (1981).
[44]W. A. Friedman, Phys. Rev. C 24, 125 (1981).
[45]S. Kubono, P. D. Bond, and C. E. Thorn, Phys. Lett. 81B, 140 (1979).
[46]Y. C. Tang, M. LeMere, and D. R. Thompson, Phys. Rep. 47, 1 (1978), and references contained therein.
[47]M. LeMere, R. E. Brown, Y. C. Tang, and D. R. Thompson, Phys. Rev. C 15, 1191 (1977).
[48]P. E. Hodgson, in *Uncertainty Principle and Foundations of Quantum Mechanics,* edited by W. C. Price and S. S. Chissick (Wiley, New York, 1977), p. 485.
[49]W. von Oertzen, Nucl. Phys. A148, 529 (1970).
[50]C. K. Gelbke, R. Bock, and A. Richter, Phys. Rev. C 9, 852 (1974).
[51]R. Stock, U. Jahnke, D. L. Hendrie, J. Mahoney, C. F. Maguire, W. F. W. Schneider, D. K. Scott, and G. Wolschin, Phys. Rev. C 14, 1824 (1976).
[52]P. E. Hodgson, *The Optical Model of Elastic Scattering* (Clarendon, London, 1963), p. 61.
[53]V. Shkolnik, M. A. Franey, and D. Dehnhard, Proceedings of the International Conference on Nuclear Physics, Berkeley, 1980, Lawrence Berkeley Laboratory Report No. LBL/11118, 1980, p. 588.
[54]M. A. Franey and P. J. Ellis, Phys. Rev. C 23, 787 (1981).
[55]R. M. Drisko, G. R. Satchler, and R. H. Bassel, Phys. Lett. 5, 347 (1963).
[56]A. M. Bernstein, in *Advances in Nuclear Physics,* edited by M. Baranger and E. Vogt (Plenum, New York, 1970), Vol. 3, p. 336.
[57]R. S. Mackintosh and A. M. Kobos, J. Phys. G 5, 359 (1979).
[58]W. E. Frahn, M. S. Hussein, L. F. Canto, and R. Donangelo, Nucl. Phys. A369, 166 (1981).
[59]K. Wildermuth and Y. C. Tang, *A Unified Theory of the Nucleus* (Academic, New York, 1977), p. 168.
[60]P. Braun-Munzinger and J. Barrette, Phys. Rep. 87, 210 (1982).